The azimuthal path of myosin V and its dependence on lever-arm length

John H. Lewis, John F. Beausang, H. Lee Sweeney, and Yale E. Goldman

The Pennsylvania Muscle Institute and Department of Physiology, University of Pennsylvania School of Medicine, Philadelphia, PA 19104

Myosin V (myoV) is a two-headed myosin capable of taking many successive steps along actin per diffusional encounter, enabling it to transport vesicular and ribonucleoprotein cargos in the dense and complex environment within cells. To better understand how myoV navigates along actin, we used polarized total internal reflection fluorescence microscopy to examine angular changes of bifunctional rhodamine probes on the lever arms of single myoV molecules in vitro. With a newly developed analysis technique, the rotational motions of the lever arm and the local orientation of each probe relative to the lever arm were estimated from the probe's measured orientation. This type of analysis could be applied to similar studies on other motor proteins, as well as other proteins with domains that undergo significant rotational motions. The experiments were performed on recombinant constructs of myoV that had either the native-length (six IQ motifs and calmodulins [CaMs]) or truncated (four IQ motifs and CaMs) lever arms. Native-length myoV-6IQ mainly took straight steps along actin, with occasional small azimuthal tilts around the actin filament. Truncated myoV-4IQ showed an increased frequency of azimuthal steps, but the magnitudes of these steps were nearly identical to those of myoV-6IQ. The results show that the azimuthal deflections of myoV on actin are more common for the truncated lever arm, but the range of these deflections is relatively independent of its lever-arm length.

The Journal of General Physiology

INTRODUCTION

Myosin V (myoV) is an unconventional myosin that exists as a dimer in cells and is able to step processively along filaments of actin for relatively large distances (~1 µm) through a cytoplasm that is densely packed (Mehta et al., 1999; Reck-Peterson et al., 2000; Sakamoto et al., 2000; Walker et al., 2000; Veigel et al., 2002; Sweeney and Houdusse, 2010). How myoV is able to navigate through such a complex environment has been the subject of several in vitro studies that focused on dissecting the basic stepping mechanism of individual myoV motors on isolated actin filaments (Rief et al., 2000; Ali et al., 2002, 2007; Forkey et al., 2003; Toprak et al., 2006; Kodera et al., 2010). myoV, as with other members of the myosin family, binds in a fixed orientation to filamentous actin (F-actin) through its N-terminal motor domain. At the C-terminal end of the motor domain is the light chain domain (LCD; also known as the lever arm), which is defined by six calmodulin (CaM)-binding IQ motifs, each bound to a CaM or CaM-like subunit. This domain amplifies small motions in the motor head associated with each ATP turnover resulting in forward motion along the actin filament track, a concept known as the swinging lever-arm hypothesis (Cooke, 1986). The LCD has been found to have additional degrees of freedom, giving the myosin conformational flexibility (Dobbie et al., 1998; Corrie et al., 1999; Veigel et al., 2002).

Because F-actin is a two-stranded right-handed helix, there is a potential for myoV to take off-axis steps that would require a high level of flexibility. Electron microscope images of myoV frozen during processive motility along F-actin indicate that its two heads bind to actin predominantly spanning 13 actin subunits, with smaller subpopulations spanning 11 and 15 subunits (Walker et al., 2000). The distance spanned by 13 actin subunits corresponds to the 36-nm half-helical repeat of F-actin, consistent with the 36-nm step size of myoV (Mehta et al., 1999). Two actin monomers 13 subunits apart have approximately the same azimuthal orientation (Amos and Amos, 1991), leading myoV to walk relatively straight by stepping typically 13 subunits (~36 nm) per step.

This view is supported by many single-molecule experiments in which myoV walks along actin bound to a rigid glass surface, which inhibits large azimuthal changes around the actin (Forkey et al., 2003; Toprak et al., 2006; Kodera et al., 2010). When myoV was observed to walk along filaments suspended away from the glass surface, though, the motors either walked straight

Correspondence to Yale E. Goldman: goldmany@mail.med.upenn.edu

Abbreviations used in this paper: BR, bifunctional rhodamine; CaM, calmodulin; DOPI, defocused orientation and position imaging; EM, electron microscopy; F-actin; filamentous actin; LCD, light chain domain; myoV, myosin V; PFI, polarized fluorescence intensity; polTIRF, polarized total internal reflection microscopy.

The Rockefeller University Press $30.00
J. Gen. Physiol. Vol. 139 No. 2 101–120
www.jgp.org/cgi/doi/10.1085/jgp.201110715

or with a gradual left-handed pitch, suggesting that the leading head of myoV lands on the 13th and, sometimes, on the 11th subunit from its trailing head (Ali et al., 2002). Twirling assays, which monitor the rotation of actin gliding along multiple motors fixed to a surface, also found that myoV walks straight along actin or it follows a gradual left-handed helical path (Beausang et al., 2008a).

Polarized total internal reflection microscopy (polTIRF) and defocused orientation and position imaging (DOPI) measurements have also shown myoV walking relatively straight (Forkey et al., 2003), with some sudden sideways tilts (Syed et al., 2006). polTIRF and DOPI are methods that directly measure the three-dimensional orientation of fluorescent rhodamine probes bifunctionally attached to a CaM (BR-CaM) bound to one of the myoV LCDs. In polTIRF, several polarized light intensities are detected and used to estimate the polar and azimuthal angles β_P and α_P, which describe the orientation of the probe's absorption and emission dipoles relative to the long axis of actin (Fig. 1 A) (Forkey et al., 2003). In DOPI, the shape of a slightly out of focus image provides the orientation of the probe (Toprak et al., 2006). These techniques have clearly demonstrated that the LCD switches between two distinct orientations associated with leading and trailing positions of the heads, providing strong support for a "hand-over-hand" stepping model (Forkey et al., 2003).

polTIRF and DOPI measurements report angles of the fluorescent probe. Because the rhodamine probe is not generally aligned with the myoV LCD, measurements of the probe orientation do not directly correspond to the orientation of the lever arm. In this paper, however, we

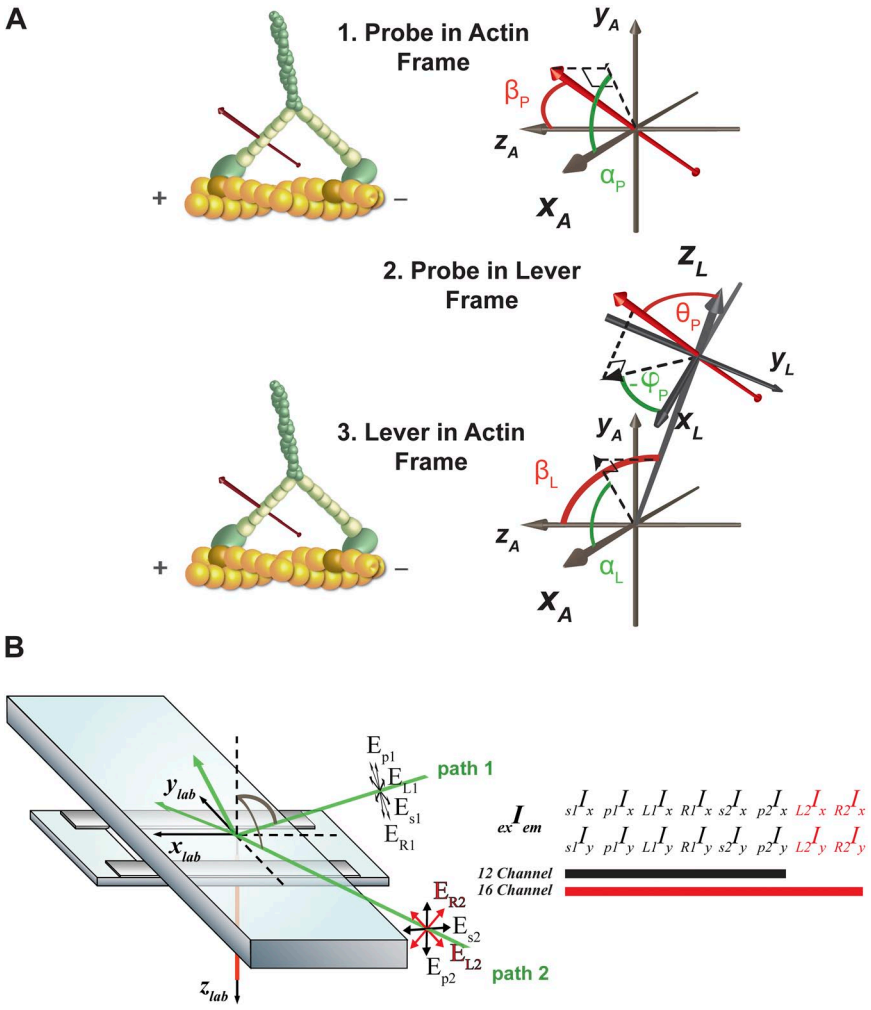

Figure 1. Schematics of relevant frames of reference and polarized intensities. (A) Definitions of the orientation of the vector representing the rhodamine probe absorption and emission dipoles, β_P, α_P, in the Actin Frame (1; x_A, y_A, z_A) and θ_P, ϕ_P, in the Lever Frame (2; x_L, y_L, z_L), which is itself shown, β_L, α_L, in the Actin Frame (3). (B) Laboratory frame: $z_{laboratory}$ is aligned in the optical axis toward the microscope objective; $x_{laboratory}$ and $y_{laboratory}$ are parallel to the slide surface. Note that the $z_{laboratory}$ and y_A axes, which are identical, point downward (Materials and methods) but are drawn pointing upward in A for clarity. Experimental setup for polTIRF microscopy: A 532-nm laser is initially split into paths 1 and 2 and is polarized using an optical setup similar to the one described in Beausang et al. (2008a). At the sample, the two beams in orthogonal planes, $x_{laboratory}$–$z_{laboratory}$ and $y_{laboratory}$–$z_{laboratory}$, alternatingly strike the quartz slide at angles (measured from the optical axis) slightly larger than the critical angle required for TIRF (Hecht, 2001). Each beam is sequentially polarized by Pockels cells into four polarizations: (1) horizontally (s1 and s2, perpendicular to the $x_{laboratory}$–$z_{laboratory}$ and $y_{laboratory}$–$z_{laboratory}$ scattering planes for paths 1 and 2, respectively); (2) in the scattering planes (p1 and p2, respectively); and (3 and 4) ±45° (L1/R1 and L2/R2, at ±45° angles with respect to the scattering plane). 12- and 16-channel measurements: Emission from the excited sample is split into its $x_{laboratory}$ and $y_{laboratory}$ components for detection by avalanche photodiodes (Materials and methods), leading to a maximum of 16 unique combinations of the eight time-multiplexed input paths and polarizations and two simultaneously detected polarized emission intensities. 12-channel measurements were made when the L and R polarizations were not used in path 2.

developed a way to determine the local angle of the probe relative to the lever arm and to use that information to calculate the actual lever-arm orientation.

The step sizes of recombinant myoV constructs with different lever-arm lengths have been shown to depend directly on the length of their LCDs (Purcell et al., 2002; Sakamoto et al., 2005). In this work, the orientation of the BR-CaM–labeled lever arm of a truncated (4IQ) and full-length (6IQ) construct was compared using polTIRF microscopy. The truncated construct, indeed, walked much less straight along actin, wobbling from side to side as it progressed. We also determined the influence of the lever-arm length on the polar rotation ("twirling") of an actin filament translocated by multiple myosins in a gliding filament assay. The truncated construct led to more frequent actin twirling, surprisingly demonstrating either left- or right-handedness.

MATERIALS AND METHODS

Preparation of proteins

G-actin was obtained from rabbit skeletal muscle (Pardee and Spudich, 1982). Biotinylated Alexa Fluor 647–labeled F-actin was prepared from G-actin, Alexa Fluor 647 actin (Invitrogen), and biotin-actin (Cytoskeleton) in a 5:1:1 ratio with 1 µM of total actin subunit concentration and stabilized with 1.1 µM phalloidin (Invitrogen). 0.3% rhodamine-labeled F-actin was prepared from unlabeled actin and 6′-IATR rhodamine-actin (Corrie and Craik, 1994) and stabilized with 1.1 µM phalloidin. Recombinant chicken myoV, with its full-length lever arm (myoV-6IQ; amino acids 1–1099) or a truncated lever arm (myoV-4IQ; amino acids 1–863) and with a FLAG affinity tag at its C terminus, was coexpressed with CaM in SF9 cells (Fig. S1) (Purcell et al., 2002). Chicken CaM, with residues Pro66 and Ala73 mutated to cysteine, was expressed in *Escherichia coli* (Putkey et al., 1985), purified, and labeled with bifunctional rhodamine (BR; provided by J.E.T. Corrie, National Institute for Medical Research, Mill Hill London, UK; Corrie et al., 1998). myoV was labeled by exchanging endogenous CaM with exogenous BR-CaM at low stoichiometry (Forkey et al., 2003).

Buffers

M5 buffer (pH 7.6) contains 25 mM KCl, 20 mM HEPES, 2 mM $MgCl_2$, and 1 mM EGTA in deionized water. $M5^+$ buffer is M5 plus 10 mM dithiothreitol (DTT) and 100 µg/ml wild-type CaM (expressed in bacteria; Putkey et al., 1985). The motility buffer for single-molecule myoV motility assays is $M5^+$ buffer plus 4 µM ATP and 50 mM DTT. The motility buffer for actin twirling assays is $M5^+$ buffer plus 100 µM ATP, 10 mM phosphocreatine (Sigma-Aldrich), 0.3 mg/ml creatine phosphokinase (prepared daily from powder; Sigma-Aldrich), and 50 mM DTT.

Experimental apparatus

In the original polTIRF setup developed in our laboratory, four time-multiplexed laser polarizations, each predominately aligned along the laboratory *x*, *y*, or *z* axis, illuminated the sample with two intersecting beam paths. The fluorescence emission was directed through a polarizing beam-splitting cube and onto two avalanche photodiodes (giving polarized detection along the *x* and *y* directions over an area corresponding to a 2-µm diameter disc at the sample) resulting in eight measured polarized fluorescence intensities (PFIs) that were used to estimate the probe orientation during every 40-ms excitation cycle. Symmetric orientations of the probe related by reflections across the Cartesian planes resulted in the same intensities, leading to an eightfold ambiguity in probe orientation (i.e., angles were limited to an octant of a sphere). In this work, additional laser polarizations aligned at ±45° between the original polarizations were included (Beausang et al., 2008a), either in one beam path for a total of 12 PFIs or in both beam paths for a total of 16 PFIs, measured in 80-ms time intervals (Fig. 1 B). The angular range determined in these two cases improved to a quarter-sphere and a hemisphere, respectively. Dipole symmetry of the probe prevents further increase in unambiguous angular detection range for polTIRF and polarized fluorescence methods in general.

As described previously (Forkey et al., 2000, 2003, 2005; Beausang et al., 2008a), polarization data from single myosin molecules was recorded and used as input to an analytical model of the probe's fluorescence emission to determine its orientation ($\theta_{laboratory}$, $\phi_{laboratory}$) in the laboratory frame of reference ($x_{laboratory}$, $y_{laboratory}$, $z_{laboratory}$), which is defined in Fig. 1 B. In general, orientations in this work are vectors represented by two polar coordinates; i.e., $\Omega \equiv$ (polar angle, azimuthal angle), where the polar angle is defined from the $+z$ axis to the vector, and the azimuthal angle is defined to the projection of the vector in the xy plane from the $+x$ toward the $+y$ axis. The probe and lever orientations in the various reference frames are summarized in Table 1.

To compare molecules moving on actin filaments aligned in different directions in the sample plane, we transformed the orientation of the probe at each time point from the laboratory frame to a frame of reference based on the actin filament (x_A, y_A, z_A) (Fig. 1 A) (Forkey et al., 2000, 2003, 2005; Beausang et al., 2008a,b). The z_A axis is aligned with the barbed (plus) end of the actin filament, which is inferred from the motion of the myosin before recording the polarization data (Beausang et al., 2008a), y_A is aligned with the optical axis pointing into the objective, and x_A lies in the sample plane perpendicular to z_A and y_A. Because of the dipole symmetry, the orientation of the probe in the actin frame is described equivalently by $\Omega_P = (\beta_P, \alpha_P)$ and

TABLE 1

List of variables

Variable	Definition
(x_A, y_A, z_A)	Axes describing actin frame of reference
$\Omega_P = (\beta_P, \alpha_P)$	Probe orientation in the actin frame
$\Omega'_P = (180° - \beta_P, \alpha_P \pm 180°)$	Probe orientation in the actin frame due to dipole symmetry
$\Omega_L = (\beta_L, \alpha_L)$	Lever orientation in the actin frame
(x_L, y_L, z_L)	Axes describing lever frame of reference
(θ_P, φ_P)	Probe orientation in the lever frame
$(x_{laboratory}, y_{laboratory}, z_{laboratory})$	Axes describing laboratory frame of reference
$(\theta_{laboratory}, \varphi_{laboratory})$	Probe orientation in the laboratory frame

$\Omega'_P = (180° - \beta_P, \alpha_P \pm 180°)$. These two orientations completely describe the probe measured with 16 PFIs, but 12-PFI data results in probe orientations that have an additional degeneracy resulting in four equivalent orientations. For convenience, the orientations of the 12 PFIs most consistent with the 16-PFI data are presented. Dwell periods for (β_P, α_P) are defined between two consecutive transitions in β_P.

Single-molecule motility assay

A precleaned fused silica slide (Corning HPFS grade; Quartz Scientific, Inc.) was further treated in an ion plasma cleaner for 5 min and then spin coated with 2 mg/ml polymethyl methacrylate (PMMA; Sigma-Aldrich) in methylene chloride. The PMMA-coated slide was assembled into a 10–20-µl flow chamber with a glass coverslip and double-sided adhesive tape. Actin was adhered to the slide and aligned approximately with $x_{laboratory}$ by successive additions and 1 min of incubations of 1 mg/ml biotinylated BSA (Sigma-Aldrich), 0.5 mg/ml streptavidin (Sigma-Aldrich), and 100 nM biotinylated Alexa Flour 647–labeled F-actin, each followed by washes with $M5^+$ buffer. myoV, containing BR-CaM, was introduced into the sample chamber at 10–1,000 pM in $M5^+$ buffer, which contains 4 µM MgATP.

Only molecules with clearly changing polarization recordings from a single probe, as indicated by step photobleaching to the fluorescence intensity baseline, were chosen for analysis, corresponding to 298 and 378 recordings for myoV-6IQ and myoV-4IQ, respectively. After determining the maximum likelihood orientation for each cycle of these recordings (described below), only molecules with at least two clear orientational steps were retained for further analysis ($n = 73$ molecules [25%] for myoV-6IQ; $n = 49$ [13%] for myoV-4IQ). The percentage of myoVs stepping twice before the photobleach is 1.9-fold higher for 6IQ than for 4IQ, which is likely related to the 1.9-fold higher run length of myoV-6IQ reported earlier (Sakamoto et al., 2005).

Actin twirling assay

A flow chamber was assembled as above, except that the fused silica slide was coated with 2.5 mg/ml poly-L-lysine (Sigma-Aldrich) instead of PMMA, and then 0.2 mg/ml anti-FLAG antibody (Sigma-Aldrich) was added and incubated for 1 min. 20 µl of ~0.2 mg/ml of unlabeled myoV-6IQ or myoV-4IQ (i.e., without BR-CaM) was flowed in and incubated for 8 min. Exposed poly-L-lysine and fused silica were blocked with 2 × 20–µl washes of 0.5 mg/ml BSA. Two 20-µl aliquots of pre-sheared, unlabeled F-actin (5 µM) were incubated for 1 min each to block any inactive myosin heads, and then unbound actin was flushed out with 20 µl of 2 mM ATP in $M5^+$ buffer. After two further washes of $M5^+$ to remove residual ATP, 5 nM actin filaments, sparsely (0.3%) labeled with rhodamine, in $M5^+$ buffer were incubated for 1 min, and then motility buffer was added to initiate filament gliding. Moving fluorescent spots were selected for polTIRF recording, and then the probe orientation was determined as described above.

Theory and analysis for transforming probe angles to lever angles

Model of myoV used in the analysis. myoV is composed of two heavy chains bound together through a coiled-coil region located past the C-terminal end of their lever arms (Reck-Peterson et al., 2000). Our simplified model of myoV treats each half of the molecule as an actin-binding motor domain connected via a compliant joint to a rigid, inextensible lever arm, which is, in turn, connected to the other half of the molecule via a free swivel at the lever-tail junction (Fig. 1 A). The orientation of the lever arm relative to the actin filament $\Omega_L = (\beta_L, \alpha_L)$ is represented by a vector pointing away from the motor domain toward the C terminus. The orientation of the probe relative to the lever-arm $\Omega_P^L = (\theta_P, \varphi_P)$ is defined in the lever (or local) frame of reference (x_L, y_L, z_L) (Fig. 1 A). The z_L axis of the lever frame is aligned with the lever-arm vector; the x_L axis is aligned along a vector defined by two residues (from C266 to F262) separated by one turn in an α helix located in the motor domain that is roughly perpendicular to the actin filament. The y_L axis is then defined as perpendicular to both the x_L and z_L axes, and its direction is given by the cross product: $y_L = z_L \times x_L$. This definition assumes that the twist of the lever arm around its long axis (the γ_L angle; Corrie et al., 1999) is constant. Values for (θ_P, φ_P) depend on the orientation of the probe bound to the CaM and on how the CaM is bound to the lever arm. Because the probe is rigidly bound to the CaM and the CaM is rigidly bound to the lever arm, we assume that the values for (θ_P, φ_P) are constant for each molecule.

A prediction of the hand-over-hand model is that the β_P and β_L angles switch between two states as the lever arm transitions back and forth between its leading and trailing positions. To the extent that the two lever arms are rigid, $\beta_{L,Leading} + \beta_{L,Trailing} = 180°$. This analysis assumes these two features. We do not necessarily expect (or observe; Fig. 4 B) only two angular values for α_P and α_L, as the azimuthal position of myoV depends on (a) the random orientation of the actin subunit to which myoV initially binds, and (b) any azimuthal changes myoV makes as it steps along the actin helix.

The change in α_P after two steps of myoV equals the corresponding change in α_L ($^2\Delta\alpha_P = {}^2\Delta\alpha_L$). Fig. 2 is a diagram of a labeled molecule of myoV stepping straight along actin, showing that even when the myosin walks straight, the azimuthal orientation of the probe relative to the actin (α_P) changes after a step because it is not, in general, located within the plane of rotation. However, α_P returns to its original orientation after a second step because the structure is identical, except for the translocation. In this simple (straight-walking) case, it is clear that the change in α_P and α_L over two steps (i.e., $^2\Delta\alpha_P$ and $^2\Delta\alpha_L$) equals zero. For more complicated steps along actin, even with changes in α_L, the two quantities are related by $^2\Delta\alpha_P = {}^2\Delta\alpha_L$ (Section 3 of the Appendix and Eq. A.37), if the change in β_P over two steps ($^2\Delta\beta_P$) is zero. In practice, $|^2\Delta\beta_P| < 10°$ is used. In summary, the assumptions of the analysis, $^2\Delta\beta_P \cong 0$ and $^2\Delta\alpha_P = {}^2\Delta\alpha_L$, are consequences of the hand-over-hand mechanism. $\beta_{L,Leading} + \beta_{L,Trailing} = 180°$ applies if the lever arms are straight.

Transforming the probe angles to lever angles. To directly transform the orientation of the probe in the actin frame (β_P, α_P) into its corresponding lever orientation (β_L, α_L), the orientation of the probe relative to the lever-arm (θ_P, φ_P) has to be determined (Fig. 1 A and Sections 1 and 2 of the Appendix). Through a series of rotation operations that align the actin frame to the probe frame (Fig. S2), the probe's vector ($\boldsymbol{v}_A$) and orientation (β_P, α_P) in the actin frame are given by (Section 1 of the Appendix):

$$\begin{aligned} v_{A,x} &= (\sin\alpha_L \cdot \cos\varphi_P + \cos\alpha_L \cdot \cos\beta_L \cdot \sin\varphi_P) \cdot \sin\theta_P + \cos\alpha_L \cdot \sin\beta_L \cdot \cos\theta_P \\ v_{A,y} &= (-\cos\alpha_L \cdot \cos\varphi_P + \sin\alpha_L \cdot \cos\beta_L \cdot \sin\varphi_P) \cdot \sin\theta_P + \sin\alpha_L \cdot \sin\beta_L \cdot \cos\theta_P \\ v_{A,z} &= -\sin\beta_L \cdot \sin\theta_P \cdot \sin\varphi_P + \cos\beta_L \cdot \cos\theta_P \end{aligned} \quad (1)$$

and

$$\begin{aligned} \beta_P(\theta_P, \varphi_P, \beta_L) &= \operatorname{acos}(v_{A,z}) \\ \alpha_P(\theta_P, \varphi_P, \alpha_L, \beta_L) &= \operatorname{atan2}(v_{A,x}, v_{A,y}) \end{aligned}. \quad (2)$$

The atan2(x, y) function is similar to atan(y/x), except that atan2 (x, y) is single valued over a larger range ($-\pi \le \alpha_P \le \pi$).

Inverting Eqs. 1 and 2 gives the lever-arm vector ($\boldsymbol{w}_A$) and orientation (β_L, α_L) in the actin frame (Section 2 of the Appendix):

$$\begin{aligned} w_{A,x} &= \left(\cos\left(\beta_L\left(\theta_P,\varphi_P,\beta_P\right)\right)\cdot\sin\varphi_P\cdot\sin\theta_P + \sin\left(\beta_L\left(\theta_P,\varphi_P,\beta_P\right)\right)\cdot\cos\theta_P\right) \\ &\cdot\cos\alpha_P - \sin\theta_P\cdot\cos\varphi_P\cdot\sin\alpha_P \\ w_{A,y} &= \left(\cos\left(\beta_L\left(\theta_P,\varphi_P,\beta_P\right)\right)\cdot\sin\varphi_P\cdot\sin\theta_P + \sin\left(\beta_L\left(\theta_P,\varphi_P,\beta_P\right)\right)\cdot\cos\theta_P\right) \\ &\cdot\sin\alpha_P + \sin\theta_P\cdot\cos\varphi_P\cdot\cos\alpha_P \\ w_{A,z} &= \left(\cos\theta_P\cdot\cos\beta_P \pm \sqrt{\sin\theta_P^{\,2}\cdot\sin\varphi_P^{\,2}\cdot\left(\sin\beta_P^{\,2} - \sin\theta_P^{\,2}\cdot\cos\varphi_P^{\,2}\right)}\right) \\ &/\cos\theta_P^{\,2} + \sin\theta_P^{\,2}\cdot\sin\varphi_P^{\,2} \end{aligned} \tag{3}$$

and

$$\begin{aligned} \beta_L\left(\theta_P,\varphi_P,\beta_P\right) &= \operatorname{acos}\left(w_{A,z}\right) \\ \alpha_L\left(\theta_P,\varphi_P,\alpha_P,\beta_P\right) &= \operatorname{atan2}\left(w_{A,x},w_{A,y}\right) \end{aligned}. \tag{4}$$

Eqs. 3 and 4 imply that calculating β_L and α_L from the measured values of β_P and α_P requires finding reliable values of (θ_P, φ_P) for each observed myoV.

Determining $\boldsymbol{\theta}_P$ and $\boldsymbol{\varphi}_P$. Differences in probe and lever-arm azimuth after one step are given by $\Delta\alpha_{P,n} = \alpha_{P,n+1} - \alpha_{P,n}$ and $\Delta\alpha_{L,n} = \alpha_{L,n+1} - \alpha_{L,n}$, respectively, where n indexes the steps ($n = 1, 2\ldots N-1$) between the N pauses in a processive run (Sections 3–5 in the Appendix). These two expressions are related by:

$$^2\Delta\alpha_{P,n} = \Delta\alpha_{P,n} + \Delta\alpha_{P,n+1} = \Delta\alpha_{L,n} + \Delta\alpha_{L,n+1} = {}^2\Delta\alpha_{L,n}, \tag{5}$$

and thus

$$\begin{aligned} \Delta\alpha_{P,n} - \Delta\alpha_{L,n} &= \Delta\alpha_{L,n+1} - \Delta\alpha_{P,n+1} \\ &= (-1)^{m-1}\left(\Delta\alpha_{P,n+(m-1)} - \Delta\alpha_{L,n+(m-1)}\right) \equiv R, \end{aligned} \tag{6}$$

where m is an integer describing the interval of steps being considered, and R is a constant for a given molecule that depends on the local probe angle (θ_P, φ_P) (Section 4 of the Appendix). When the molecule walks straight ($\Delta\alpha_L = 0$), $R = |\Delta\alpha_P|$.

Our strategy for calculating (θ_P, φ_P) requires finding an estimate for R so as to calculate the $N-1$ values of $\Delta\alpha_{L,n}$ to use in the following system of equations based on Eqs. 3 and 4 (Section 5 of the Appendix):

$$\alpha_L\left(\theta_P,\varphi_P,\alpha_{P,n+1},\beta_{P,n+1}\right) - \alpha_L\left(\theta_P,\varphi_P,\alpha_{P,n},\beta_{P,n}\right) = \Delta\alpha_{L,n} \tag{7}$$

$$\beta_L\left(\theta_P,\varphi_P,\beta_{P,n+1}\right) + \beta_L\left(\theta_P,\varphi_P,\beta_{P,n}\right) = {}^{Tot}\beta_{L,n}. \tag{8}$$

The value for R for each molecule is obtained by calculating the average of $(-1)^n\cdot\Delta\alpha_P$ over all n. If $\Delta\alpha_L$ is zero or a constant for a processive run, this average exactly equals R (Section 4 of the Appendix). $\Delta\alpha_L$ (and by extension, $|\Delta\alpha_P|$) is <u>not</u> generally constant, so a weighted average of $(-1)^n\cdot\Delta\alpha_P$ (i.e., $\overline{\Delta\alpha_P}$) is calculated that deemphasizes values of $\Delta\alpha_P$ that occur when the molecule takes large sideways steps that are atypical:

$$\overline{\Delta\alpha_P} = \frac{\sum_{n=1}^{N-1}(-1)^n\cdot W_n\cdot\Delta\alpha_{P,n}}{\sum_{n=1}^{N-1}W_n} \cong R, \tag{9}$$

with the following definition for the weighting function, W (Section 4 of the Appendix):

$$W_n = \frac{1}{\left(\left|\Delta\alpha_{P,n} - \overline{\Delta\alpha_P}\right| + \varepsilon\right)^r}, \tag{10}$$

where a small value, ε, is chosen to avoid division by 0, and r is an even positive integer. The results of the procedure are not sensitive to the values of ε and r. Setting them to $\varepsilon = 0.0001$ rad and $r = 4$ results in a robust stable value of R for each molecule.

Given $N-1$ values of $\Delta\alpha_P$ measured from a molecule taking N steps along actin, Eq. 9 is used to calculate an approximation for R. This value for R is then applied in Eq. 6 to calculate the $N-1$ corresponding values for $\Delta\alpha_L$. θ_P and φ_P are then adjusted in Eqs. 7 and 8 using the $N-1$ values of $\Delta\alpha_L$ and ${}^{Tot}\beta_{L,n} = \beta_{L,n} + \beta_{L,n+1} = 180°$, assuming that the lever arm is straight in both the leading and trailing positions. Once an estimate for (θ_P, φ_P) is obtained for that molecule, β_L and α_L are calculated using Eqs. 3 and 4 and the N measured values of β_P and α_P.

Treatment of degeneracy of probe orientation for myoV undergoing multiple $\boldsymbol{\beta}_P$ transitions. When using 16 channels of polarized intensity, the solution of the probe's orientation $\Omega_P \equiv (\beta_P, \alpha_P)$ is limited to a hemisphere of orientation, which is set to be $0° \le \beta_P \le 90°$ and $-180° \le \alpha_P \le 180°$. Because of the symmetry of the dipole

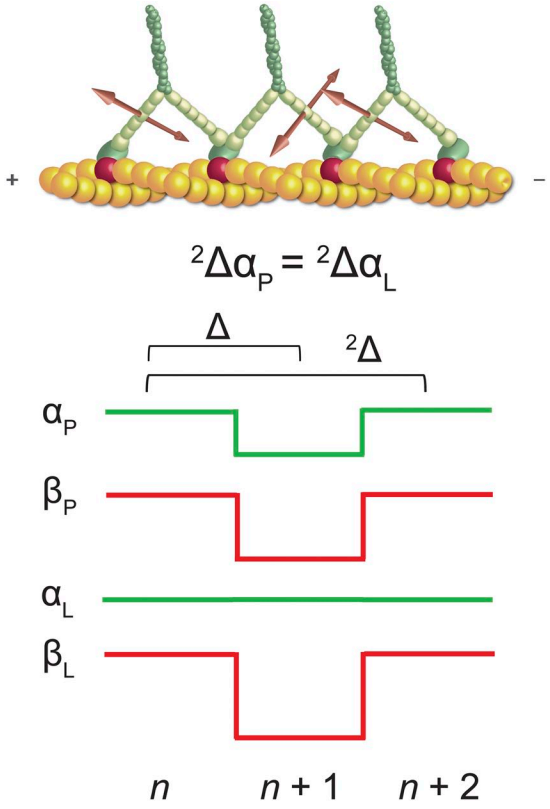

Figure 2. Schematic explanation of ${}^2\Delta\alpha$. The azimuthal changes in probe angle, α_P, and lever angle, α_L, over two steps are referred to as ${}^2\Delta\alpha_P$ and ${}^2\Delta\alpha_L$, respectively. When walking straight, the probe attached to the myoV lever arm returns to its original orientation every two steps, so that both ${}^2\Delta\alpha_P$ and ${}^2\Delta\alpha_L$ equal zero and ${}^2\Delta\alpha_P = {}^2\Delta\alpha_L$. It can be shown that ${}^2\Delta\alpha_P = {}^2\Delta\alpha_L$ is a general relationship, regardless of straight walking, so long as β_P switches regularly between two states (Section 3 of the Appendix).

$(\Omega'_P \equiv (180° - \beta_P, \alpha_P \pm 180°))$, the probe has an equivalent orientation in the hemisphere defined by $90° \le \beta_P \le 180°$ and $-180° \le \alpha_P \le 180°$ (Forkey et al., 2000). As mentioned in the last section, β_P regularly switches between two angular states as myoV takes $N - 1$ steps along actin. These two states, along with the twofold dipole symmetry, lead to four equivalent expressions for the N measured orientations of the probe. We express these four equivalent orientations as $N - 1$ pairs consisting of two sequential angular states: $(\Omega_{P,n}, \Omega_{P,n+1})$, $(\Omega_{P,n}, \Omega'_{P,n+1})$, $(\Omega'_{P,n}, \Omega_{P,n+1})$, and $(\Omega'_{P,n}, \Omega'_{P,n+1})$.

These four equivalent probe pairs can be used to calculate four corresponding pairs of the lever-arm orientation for the N angular states of $\Omega_{L,n} \equiv (\beta_{L,n}, \alpha_{L,n}) \equiv (\beta_L(\Omega_{P,n}, \theta_P, \varphi_P), \alpha_L(\Omega_{P,n}, \theta_P, \varphi_P))$ (Eqs. 3 and 4). Solutions for $\alpha_{L,n}$ are the same for these four angular paths, but for $\beta_{L,n}$, there are two solutions that result in the different lever-arm configurations, A and B (Fig. S3). Lever-arm configuration A is calculated from the probe angle pairs $(\Omega_{P,n}, \Omega_{P,n+1})$ and $(\Omega'_{P,n}, \Omega'_{P,n+1})$ using the local probe orientations (θ_P, φ_P) and $(180° - \theta_P, \varphi_P \pm 180°)$, respectively (Fig. S3 A); configuration B is similarly calculated from the probe angle pairs $(\Omega_{P,n}, \Omega'_{P,n+1})$ and $(\Omega'_{P,n}, \Omega_{P,n+1})$ (Fig. S3 B). In general, there is not a straightforward relationship between these two lever-arm configurations except for the relationship between the local probe angles (Ω_P and Ω'_P).

For each of the four configurations described above, there is an additional equivalent solution for the lever-arm orientation that corresponds to their mirror images (Fig. S4). Given any probe solution $\Omega_{P,i}$, two equivalent lever solutions $(\Omega_{L,n} = \Omega'_{L,n})$ can be calculated that satisfy Eqs. 7 and 8, where $\Omega_{L,n}$ is described above and $\Omega'_{L,n} \equiv (180° - \beta_{L,n}, \alpha_{L,n} \pm 180°) \equiv (\beta_L(\Omega_{P,n}, \theta'_P, \varphi'_P), \alpha_L(\Omega_{P,n}, \theta'_P, \varphi'_P))$, where $\theta'_P = 180° - \theta_P, \varphi'_P = 180° - \varphi_P$. Note that this symmetry is independent of the dipole symmetry of the probe; so with this mirror symmetry and the four lever solutions related to the dipole symmetry, there are a total of eight possible related solutions for the lever-arm orientation.

Online supplemental material

Fig. S1 provides a basic schematic of the myoV-6IQ and myoV-4IQ recombinant constructs. Fig. S2 describes the different rotation operations performed by the rotation matrix used in deriving Eqs. 1 and 2 (Section 1 of Appendix). Figs. S3 and S4 demonstrate the degeneracy of the lever angle solution (Materials and methods). Figs. S5, S8, and S9 give various probe and lever angle distributions for myoV-6IQ measured using 16 PFIs (Materials and methods). Tables S1–S3 give the best-fit values from the Gaussian fits to these distributions. Figs. S6 and S7 give the distributions for $\Delta\alpha_P$ and ${}^2\Delta\beta_P$ for myoV-6IQ and myoV-4IQ. Table S4 gives the values from the Gaussian fits to these distributions. Fig. 10 illustrates the twirling experiment. Fig. S11 and Table S5 compare the polTIRF data from myoV-6IQ and myoV-4IQ to a molecular model of myoV (Parker et al., 2009). The supplemental material is available at http://www.jgp.org/cgi/content/full/jgp.201110715/DC1.

RESULTS

Measurements of the three-dimensional orientation of myoV-6IQ and myoV-4IQ during single-molecule processive motility

polTIRF measurements were made with BR probes (Forkey et al., 2003, 2005) bound to CaM subunits on two recombinant constructs of myoV derived from chicken: myoV-6IQ with its native number of CaMs (six) bound, and myoV-4IQ, truncated to contain four CaMs (Purcell et al., 2002). Both constructs have a coiled-coil region at the C terminus for dimerization but no cargo-binding domain (Fig. S1). Probe angular measurements

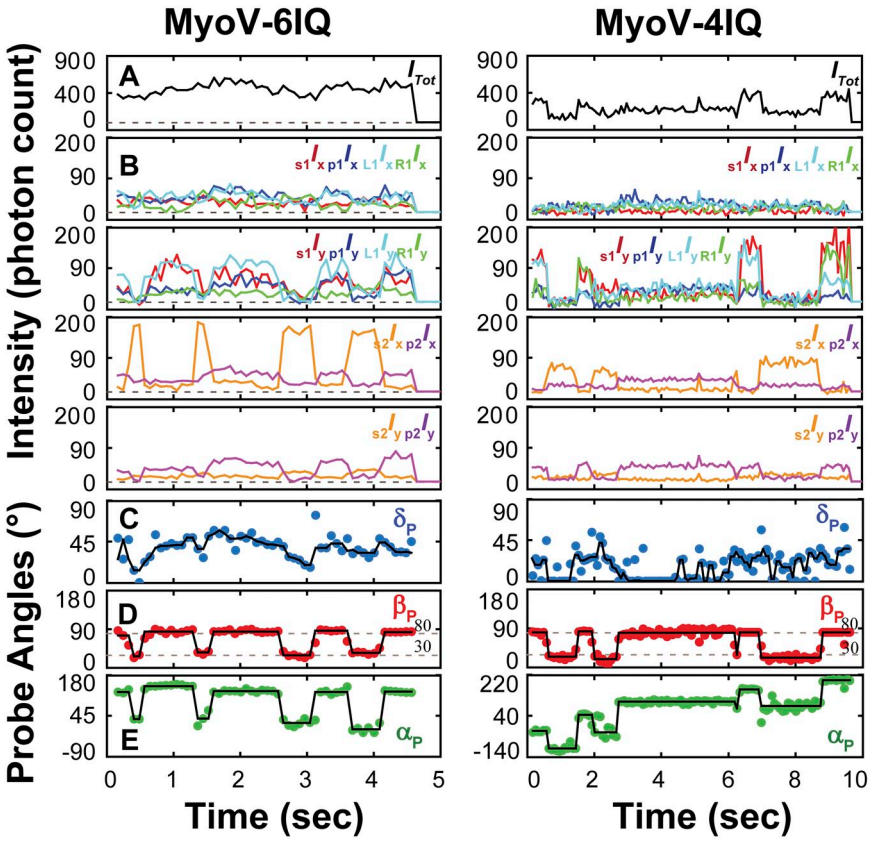

Figure 3. Representative traces from the processive runs of rhodamine-labeled myoV-6IQ (left) and myoV-4IQ (right) motors along actin filaments. (A and B) Measured intensities: The total measured intensity is shown (A), along with its 12 component intensities (B). When the rhodamine probe bleached, all of the intensities dropped to baseline. (C–E) Calculation of the orientation of the probe in the actin frame of reference: Traces of the angles δ_P, microsecond wobble (C), β_P, probe axial angle (D), and α_P, probe azimuthal angle (E) in the actin coordinate frame.

for most of the data were made using 12 PFI channels (Figs. 1 B and 3–8, and Tables 2–4); further data for myoV-6IQ was taken using 16 PFI channels (Figs. S5–S9 and Tables S1–S4). Full sets of these PFIs were recorded at 80-ms intervals.

Video sequences of BR on single myoV molecules moving processively on actin attached to the microscope slide gave average translocation velocities, V_{ave}, of 103 ± 3 nm/s (mean ± SEM; $n = 92$) and 85 ± 3 nm/s ($n = 50$) for myoV-6IQ and myoV-4IQ, respectively, at 4 µM MgATP, consistent with prior findings (Cheney et al., 1993). Representative recordings of the 12 individual polTIRF intensities (Fig. 3) for myoV-6IQ and myoV-4IQ stepping at 4 µM MgATP show that the individual traces are typically stable for periods of several hundred milliseconds and then suddenly transition, back and forth, to new intensity levels (Fig. 3 B). Complementary changes among the 12 traces result in the total intensity remaining relatively constant (Fig. 3 A). The dwell periods were exponentially distributed with mean dwell times of 702 ± 23.7 ms (mean ± SEM) and 927 ± 53.6 ms for myoV-6IQ and myoV-4IQ, respectively. The polar (Fig. 3 D, β_P) and azimuthal (Fig. 3 E, α_P) angles of the BR probe relative to the actin, calculated from the polTIRF data as described in Materials and methods, show regular switching between two orientations. The wobble angle, δ_P, is noisy (Fig. 3 C) but relatively stable. These features of the polTIRF recordings are consistent with hand-over-hand motility generated by tilting lever arms in both constructs.

Probe orientation distributions for myoV-6IQ and myoV-4IQ are similar

The traces of the axial and azimuthal angles of the probe, β_P and α_P, respectively, are stable during dwell periods. Mean values of β_P and α_P, calculated over these stable intervals, are plotted as histograms, where the β_P distribution is fit to two Gaussian components (Fig. 4). The two components of the β_P histogram, corresponding to the leading and trailing head positions, peak at 80° and 25° for myoV-6IQ, respectively, and 81° and 31° for myoV-4IQ (Fig. 4 A and Table 2). Note that an orientational ambiguity as a result of the symmetry of the optical dipoles limits expression of these probe angles to the range of 0°–90°, a restriction that does not apply to calculations of lever-arm angles given later. The values for β_P are similar to those reported previously (Forkey et al., 2003; Toprak et al., 2006), when this orientational ambiguity is considered (Materials and methods).

α_P usually visits two values during individual runs of myoV-6IQ and multiple values for myoV-4IQ (Fig. 3 E). Distributions of α_P from many processive runs of both constructs are broad (Fig. 4 B), most likely because the starting azimuth depends randomly on which actin subunit the myoV initially binds. To better understand the nature of the azimuthal paths and to eliminate the variability generated by the starting subunit, we instead consider changes in α_P as myoV steps along actin. These changes are independent of the starting azimuth.

$^2\Delta\alpha_P$ and $^2\Delta\beta_P$ distributions for myoV-6IQ and myoV-4IQ

The change of the azimuthal angle of the probe after one step of myoV, $\alpha_{P,n+1} - \alpha_{P,n}$, is termed $\Delta\alpha_P$ (Fig. 2). One should note that even if the molecule walks straight along actin, $\Delta\alpha_P$ will generally be nonzero because the BR probe is not located directly in the plane of lever-arm rotation. However, the quantity $^2\Delta\alpha_P = \alpha_{P,n+2} - \alpha_{P,n}$, the change in α_P after two steps, does reproduce the azimuthal change of the lever arm because in hand-over-hand motion, the molecule returns to the same state every other step, except for the axial translation and any accumulated azimuthal motion.

The azimuthal angle of the probe, α_P, is related to that of the lever arm of myoV, α_L, through the expression $^2\Delta\alpha_P = {}^2\Delta\alpha_L$ (Section 3 of the Appendix). This equality between $^2\Delta\alpha_P$ and $^2\Delta\alpha_L$ is a general one, independent of the local orientation of the probe with respect to the lever arm (given by polar angle θ_P and local azimuth φ_P;

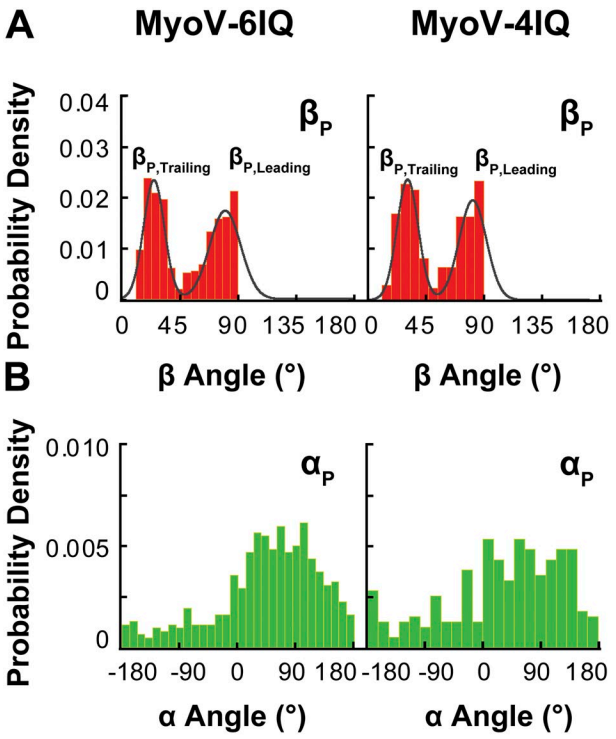

Figure 4. β_P and α_P distributions for myoV-6IQ and myoV-4IQ. Histograms of the β_P and α_P angles were collected from the mean angles in states that were visited during individual runs of myoV-6IQ (top: $n = 73$ molecules and states = 515) and myoV-4IQ (bottom: $n = 49$ molecules and states = 246). The beginning and end of each dwell were defined by the transitions in β_P. Histograms are normalized so that the total area of the distribution is equal to one. (A) β_P distributions: Each of these distributions was best fit by a bimodal Gaussian equation; the resulting parameters are given in Table 2. (B) α_P distributions.

TABLE 2

Analysis of the distributions of probe α and β angles for myoV-6IQ and myoV-4IQ in the actin frame of reference

Variable	myoV-6IQ	myoV-4IQ
	β_P angles (°)	
$\beta_{Leading}$	80 ± 12 (52%)	81 ± 11 (51%)
$\beta_{Trailing}$	25 ± 8.0 (48%)	31 ± 8.3 (49%)
	$^2\Delta\alpha_P$ angles (°)	
$^2\Delta\alpha_1$	−30 ± 27 (31%)	NA
$^2\Delta\alpha_2$	−2.0 ± 14 (50%)	−9.7 ± 88 (100%)
$^2\Delta\alpha_3$	34 ± 27 (19%)	NA

Values result from fitting a Gaussian model to the distributions and report peak ± σ.

Fig. 1 A), with the single condition that the change in β_P over two steps ($^2\Delta\beta_P$) must be equal or near to zero, as expected in a hand-over-hand mechanism (Materials and methods). The measured $^2\Delta\beta_P$ distributions for myoV-6IQ and myoV-4IQ are narrow and centered on zero (Fig. S7 and Table S4), indicating that this condition is satisfied in our measurements. The $^2\Delta\alpha_P$ distribution for myoV-6IQ has one principle peak at −2.0 ± 14° (peak ± σ) corresponding to straight walking by the motor 13 actin monomers per step. Two shoulders on either side of the central peak can be fitted by further Gaussian peaks at −30 ± 27° and +34 ± 27° (Fig. 5 A and Table 2), where the widths of the side components were constrained to be equal. This three-peak distribution fits the data better than a single Gaussian component ($P < 0.0001$, as determined by an F-test). The two side lobes in the myoV-6IQ $^2\Delta\alpha_P$ distribution correspond approximately to the motor stepping 11 or 15 subunits for one of the steps. Two Gaussian peaks (at −2.7 ± 12° and −6.9 ± 39°) also fit the data. The central peak is the same and the overlapping wider component corresponds to the two side lobes discussed above. In contrast, the $^2\Delta\alpha_P$ distribution of myoV-4IQ (Fig. 5 B) is much broader without distinct subcomponents. A single Gaussian peak, −9.7 ± 88° (Table 2), describes the histogram of myoV-4IQ $^2\Delta\alpha_P$.

Multiple subpopulations in the distributions of θ_P versus φ_P for myoV-6IQ and myoV-4IQ

The orientation of the BR probe relative to a frame of reference fixed within the lever arm is described by the polar angles (θ_P, φ_P) (Materials and methods and Fig. 1 A). Using analytical relationships between the orientation of the probe (β_P, α_P) and lever-arm (β_L, α_L) relative to actin and (θ_P, φ_P) (Eqs. 7 and 8), we can estimate (θ_P, φ_P) from the β_P and α_P angles measured from a series of steps of myoV in a processive run. This estimation arises from the relationship $^2\Delta\alpha_P = {}^2\Delta\alpha_L$ (when $^2\Delta\beta_P \cong 0$) and the further assumption that the two lever arms are rigid, leading to the relationship $^{Tot}\beta_L = \beta_{L,Trailing} + \beta_{L,Leading} = 180°$, where $\beta_{L,Trailing}$ and $\beta_{L,Leading}$ are the axial angles corresponding to the two head positions.

Scatter plots of θ_P versus φ_P calculated from individual runs of myoV-6IQ and myoV-4IQ each show three fairly distinct populations (Fig. 6 A). Each of these groups was separately binned into two-dimensional histograms and fit by two-dimensional Gaussian functions, giving peak values of (θ_P, φ_P) = (45°, −110°), (43°, −73°), and (63°, −65°) for myoV-6IQ (Table 4). The distribution of calculated values of (θ_P, φ_P) for myoV-4IQ was quite similar, also demonstrating three apparent populations peaking at (43°, −113°), (46°, −60°), and (65°, −62°) (Table 4). We tentatively hypothesize that these components of the (θ_P, φ_P) distributions for the two constructs correspond to different CaM subunits that exchanged with BR-CaM during labeling.

β_L and α_L were then calculated from the measured values of β_P and α_P, the estimated (θ_P, φ_P) for each molecule, and Eqs. 3 and 4. Representative traces of β_L and α_L (Fig. 6 B) indicate that myoV-6IQ walks hand-over-hand along actin with little azimuthal deviation (α_L is constant), sporadically exhibiting sideways motions, as described previously (Syed et al., 2006). myoV-4IQ displays similar values for β_L to those of myoV-6IQ but has a variable α_L, wandering azimuthally around actin as it walks. Distributions of $\beta_{L,Trailing}$ and $\beta_{L,Leading}$ values for myoV-6IQ (n = 73 traces) and myoV-4IQ (n = 49 traces; Fig. 7 A) show similar pairs of peaks for the two constructs. Distributions of α_L for both constructs are broad, as expected again because of their random starting azimuthal positions (Fig. 7 B).

There are two possible unique solutions for the lever angles that describe different lever-arm configurations, A and B (Materials and methods and Fig. S3). The distributions of β_L calculated for these two configurations

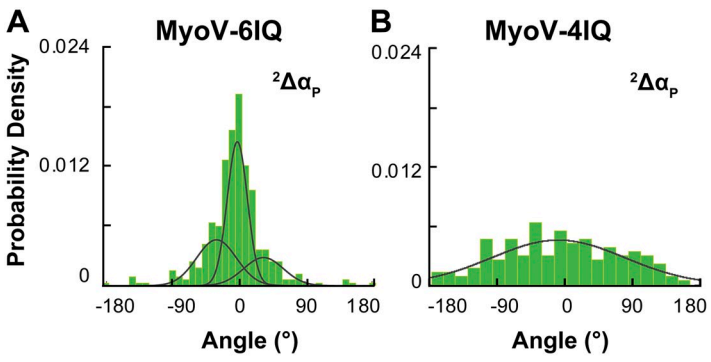

Figure 5. $^2\Delta\alpha_P$ distributions for myoV-6IQ and myoV-4IQ. Histograms of the $^2\Delta\alpha_P$ angles were calculated from the mean angles of α_P that were visited during runs of myoV-6IQ (A) and myoV-4IQ (B) and normalized as in Fig. 4. The distributions were fit by a trimodal (6IQ) or a unimodal (4IQ) Gaussian equation; the resulting parameter values are given in Table 2.

for myoV-6IQ (measured with 16 channels) each have two distinct peaks that are not substantially different (Fig. S5 A and Table S2). Therefore, although there are four equivalent probe orientations from a given run of a labeled myoV, each of these results in roughly similar values for β_L, thus reducing the final degeneracy of lever-arm orientation from eightfold to twofold. Of these two possible solutions, we eliminate one by assuming that there is not enough clearance for myoV to walk between the actin filament and the slide. Based on this assumption, we then accept the lever orientations that place the molecule on the solution side of the actin filament away from the glass (i.e., $0° < \alpha_L < 180°$) (Fig. S5 B).

Most of our data were measured using 12 channels of polarized intensity, which limits the probe to a quarter-sphere of space and leads to further degeneracies in the probe and lever-arm orientations, as mentioned earlier. We present a single solution for the 12-channel data for each molecule by constraining the probe and lever orientations to be close to those found for the 16-channel myoV-6IQ data.

$\Delta\alpha_L$ distributions for myoV-6IQ and myoV-4IQ

Distributions of $\Delta\alpha_L$ ($= \alpha_{L,n+1} - \alpha_{L,n}$), calculated from (α_P, β_P) and (θ_P, φ_P) for each molecule (Fig. 8), report the azimuthal changes of the lever arms after single steps of myoV along actin. The sign for $\Delta\alpha_L$ is negative when myoV walks leftward, at or near zero when myoV walks straight, and positive when walking rightward. The distribution of $\Delta\alpha_L$ values from myoV-6IQ data has a single principle peak at $-1.8 \pm 13°$ and two apparent shoulders at $-29 \pm 34°$ and $+33 \pm 34°$ (Fig. 8 A and Table 3), where the widths of the two side components were constrained to be equal. The straight-walking component of steps ($\Delta\alpha_L = -1.8°$) makes up ~55% of the total population. The $\Delta\alpha_L$ distribution for myoV-4IQ also has three populations with peak values very similar to those from the myoV-6IQ distributions ($\Delta\alpha_L = -35 \pm 29°$, $-1.4 \pm 10°$, and $+47 \pm 29°$; Fig. 8 B and Table 3), where the widths of the side components were constrained to be equal. These three-peak distributions fit the data better than single Gaussian components ($P < 0.0001$ for both 6IQ and 4IQ, as determined by an F-test). As with the myoV-6IQ $^2\Delta\alpha_P$ distribution described earlier, two Gaussian-centered peaks with different widths (at $-2.3 \pm 46°$ and $-1.9 \pm 12°$ [6IQ]; $-3.3 \pm 54°$ and $-1.9 \pm 8.7°$ [4IQ]) also fit the data. The central peaks are the same, and the overlapping wider components correspond to the two side lobes. The straight-walking population from the myoV-4IQ distribution ($\Delta\alpha_L = -0.2°$) makes up only 36% of the total population, much less than that for myoV-6IQ. Thus, an individual molecule of myoV-4IQ is more likely to take steps to the left or right than to walk straight.

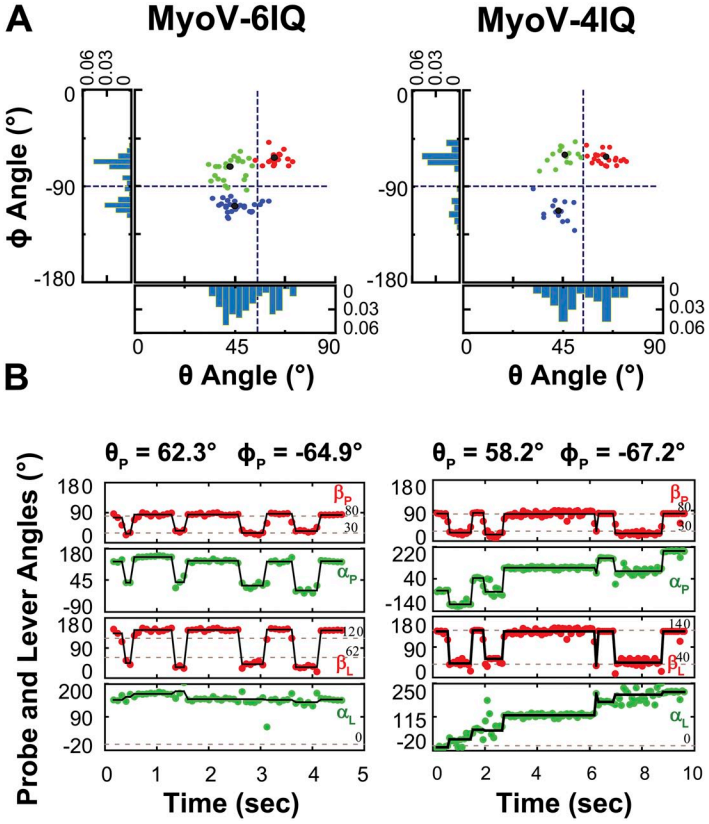

Figure 6. θ_P versus φ_P distributions for myoV-6IQ and myoV-4IQ. (A) θ_P versus φ_P distributions calculated from individual processive runs of myoV-6IQ (left; $n = 73$ molecules) and myoV-4IQ (right; $n = 49$ molecules) describing the orientation of the probe in the lever frame of reference. One-dimensional histograms of θ_P and φ_P are displayed to the left and below them. (B) Representative traces of β_L and α_L, the orientation of the lever arm in the actin reference frame, calculated from the β_P and α_P traces shown in Fig. 3 along with the corresponding values for θ_P and φ_P in those molecules (6IQ: $\theta_P = 62°$ and $\varphi_P = -65°$; 4IQ: $\theta_P = 42°$ and $\varphi_P = -124°$).

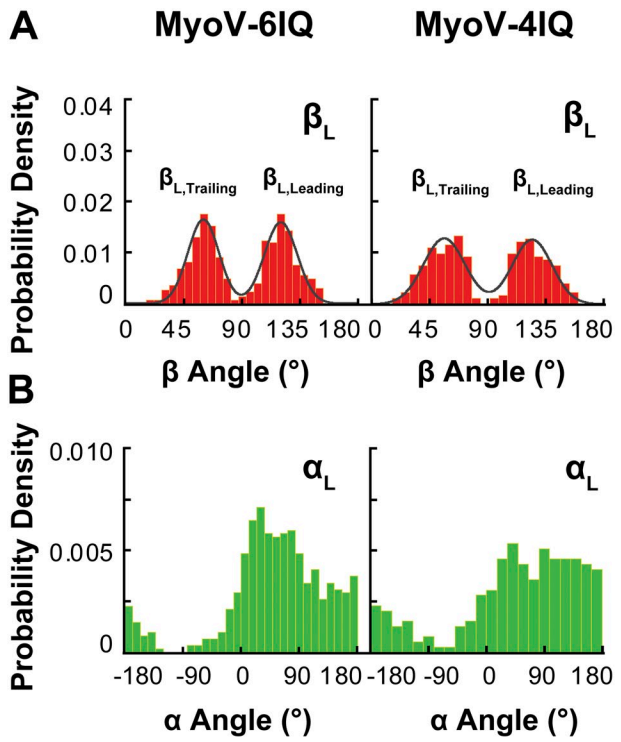

Figure 7. β_L and α_L distributions for myoV-6IQ and myoV-4IQ. Histograms of the β_L and α_L, mean angles visited during individual runs of myoV-6IQ (top: n = 73 molecules and states = 515) and myoV-4IQ (bottom: n = 49 molecules and states = 246). Dwell period selection and normalization as in Fig. 3. (A) β_L distributions: Each of these distributions was fit by a bimodal Gaussian equation; the resulting parameters are given in Table 3. (B) α_L distributions.

TABLE 3

Analysis of the distributions of lever-arm α and β angles for myoV-6IQ and myoV-4IQ in the actin frame of reference

Variable	myoV-6IQ	myoV-4IQ
	β_L angles (°)	
$\beta_{Leading}$	120 ± 12 (50%)	124 ± 15 (52%)
$\beta_{Trailing}$	60 ± 13 (50%)	56 ± 16 (48%)
	$\Delta\alpha_L$ angles (°)	
$\Delta\alpha_1$ (L)	−29 ± 34 (25%)	−35 ± 29 (36%)
$\Delta\alpha_2$ (S)	−1.8 ± 13 (55%)	−1.4 ± 10 (36%)
$\Delta\alpha_3$ (R)	33 ± 34 (20%)	47 ± 29 (28%)

Values result from fitting a Gaussian model to the distributions and report peak ± σ.

Twirling of actin in gliding assays with myoV-6IQ and myoV-4IQ

Unlabeled myoV-6IQ or myoV-4IQ was attached to the microscope slide using a C-terminal Flag tag (Fig. S1) and anti-Flag antibody. Actin, very sparsely labeled with (monofunctional) rhodamine (Materials and methods), glided on the myosin (Fig. S10) with velocity of 112 ± 5.8 and 133 ± 7.0 nm/s for myoV-6IQ and myoV-4IQ, respectively, at 0.1 mM MgATP. The angle of the fluorescent probe in actin was determined during gliding by recording 16 PFIs (Materials and methods) (Beausang et al., 2008a). As with the other myosins measured in the twirling assay, for both myoV-6IQ and myoV-4IQ, the polTIRF intensities gradually rose and fell, and the individual polarizations exhibited various relative phase shifts (Fig. 9 B). Total intensity was constant until the probe photobleached, indicating that the changes of the individual polTIRF traces are caused by probe rotation as the actin twirled around its axis during gliding (Beausang et al., 2008a). β_P often changed very little over the course of the experiment, as expected from a probe fixed to the actin (Fig. 9 D). On the other hand, α_P decreased at a constant rate with myoV-6IQ and either steadily increased or decreased with myoV-4IQ (Fig. 9 E). For each actin filament, we calculated that the pitch = V/ω of twirling, where V is the average linear velocity (nm · s^{-1}) of gliding and ω is the angular velocity (rotations · s^{-1}) calculated from $\Delta\alpha_P/\Delta t$. Inasmuch as some of the filaments did not twirl (as was also found before for myosins II, V, and VI; Sun et al., 2007; Beausang et al., 2008a), we calculated the inverse pitch (pitch^{-1} (μm^{-1})) to display distributions of both twirling and non-twirling filaments on single distributions (Fig. 10). Larger values for the inverse pitch indicate tighter twirling, and positive and negative signs indicate right- and left-handed twirling, respectively.

myoV-6IQ and myoV-4IQ show two clear differences in their twirling. A significant portion of filaments gliding over myoV-6IQ–coated surfaces did not twirl (|pitch^{-1}| < 0.4 μm^{-1} = 50%), whereas most filaments

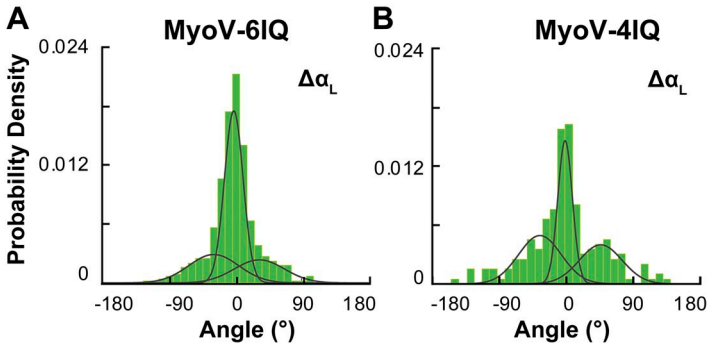

Figure 8. $\Delta\alpha_L$ distributions for myoV-6IQ and myoV-4IQ. Histograms of the $\Delta\alpha_L$ angles calculated from the mean angles of α_L that were visited during individual runs of myoV-6IQ (A) and myoV-4IQ (B). The histograms are normalized to one. Each of these distributions was fit by a trimodal Gaussian equation; the resulting parameters are given in Table 3.

TABLE 4

Analysis of the θ_P versus φ_P distributions calculated from the processive runs of myoV-6IQ and myoV-4IQ

Probe position	θ_P (°)	φ_P (°)	% Total
		myoV-6IQ	
1	45.2 ± 7.67	−110 ± 5.12	38
2	43.2 ± 7.96	−73.0 ± 12.8	28
3	63.0 ± 4.05	−64.9 ± 7.06	34
		myoV-4IQ	
1	42.9 ± 5.39	−113 ± 11.1	26
2	45.9 ± 5.71	−59.8 ± 8.83	45
3	64.5 ± 6.59	−61.9 ± 4.45	29

Values result from fitting a Gaussian model to the distributions and report peak ± σ.

on myoV-4IQ slides twirled ($|\text{pitch}^{-1}| < 0.4\ \mu m^{-1}$ = 6%). From those filaments that did twirl, a left-handed pitch of 1.4 ± 0.13 µm (mean ± SEM) was calculated, in agreement with earlier measurements on native myoV (Beausang et al., 2008a). When the pitches of both the twirling and non-twirling filaments from myoV-6IQ are considered, an average left-handed pitch of 2.7 ± 0.64 µm is calculated. myoV-4IQ, surprisingly, twirls either to the left (56%) or to the right (38%), with pitches of 1.2 ± 0.14 µm and 1.0 ± 0.19 µm, respectively. myoV-4IQ is the first myosin tested that can twirl robustly with either handedness, suggesting a coupling between the step sizes and azimuthal changes among motors mechanically connected through actin and the glass slide.

DISCUSSION

Truncating the lever arm of myoV increases off-axis steps

In this study, we were able to calculate the changes in orientation of the lever arm of myoV as it steps along actin using a novel analysis method. Previous single-molecule studies using polTIRF characterized the angular changes of fluorescent probes on the lever arm, denoted α_P and β_P, associated with stepping by myoV (Forkey et al., 2003; Syed et al., 2006; Toprak et al., 2006), but they did not transform these angles into the actual orientation of the lever arm, α_L and β_L, because the local orientation of the probe relative to the lever was generally unknown. The gradual azimuthal change as myoV travels over several steps (>1 µm), as measured by its helical pitch, has been measured in other single-molecule (Ali et al., 2002) and ensemble studies (Beausang et al., 2008a), but these earlier studies did not quantify the step-by-step changes in its azimuth, as measured by $\Delta\alpha_L$. We were able to calculate distributions for $\Delta\alpha_L$ from the present measurements of the orientation of the probe attached to individual myoVs. The native myoV construct, myoV-6IQ, predominantly

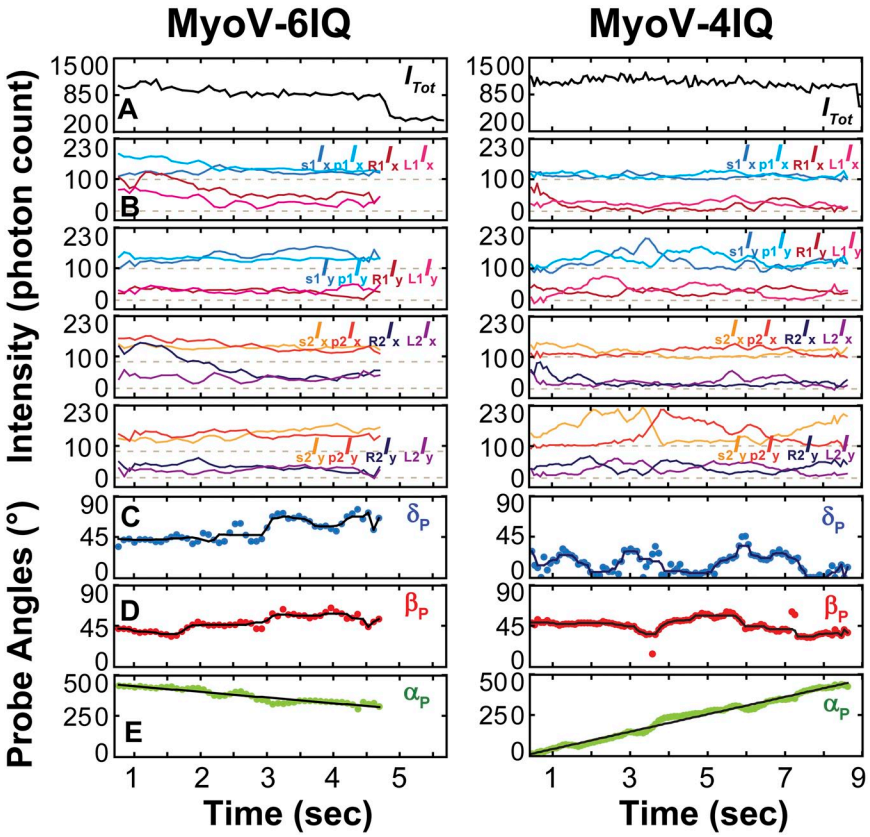

Figure 9. Representative traces from rhodamine-labeled actin filaments twirling over myoV-6IQ (left) or myoV-4IQ (right). Measured intensities (A and B): The total measured intensity is shown (A), along with its 16 component intensities (B). The rhodamine probe bleached when the intensities dropped to baseline. (C–E) Calculation of the orientation of the probe in the actin frame of reference: Traces of the angles δ_P (C), β_P (D), and α_P (E) in the actin frame. Note that α_P declines linearly for myoV-6IQ, indicating left-handed twirling, and that α_P increases linearly for myoV-4IQ, indicating right-handed twirling in this particular molecule.

takes straight steps, as indicated by the near-zero primary peak that makes up 55% of the $\Delta\alpha_L$ distribution (Fig. 8 and Table 3). This high likelihood for taking a straight step agrees well with the results from the ensemble-level gliding assays, where 50% of the actin filaments did not twirl (i.e., they moved straight) (Fig. 10), as was observed previously for tissue-purified myoV (Beausang et al., 2008a). Small shoulders to the left and right of the principle $\Delta\alpha_L$ peak, at $-29°$ and $+33°$ (Fig. 8), account for the remainder of the $\Delta\alpha_L$ distribution, where leftward steps ($\Delta\alpha_L < 0$) are found almost twice as often as rightward steps ($\Delta\alpha_L > 0$) (Table 3). This leftward stepping is in agreement with the behavior of the other 50% of the observed filaments in the gliding assay, which twirled with a left-handed pitch (Figs. 9 and 10), as observed previously (Ali et al., 2002; Beausang et al., 2008a). From the entire $\Delta\alpha_L$ distribution, the average change in α_L is $-2.3°$ per step. With an average step size of 36 nm, the helical path is predicted to be left-handed with a pitch of 5.6 µm ($360° \cdot 36$ nm$/2.3°$). This value is approximately twofold larger than the overall average pitch we found in the ensemble gliding assays and what was reported by Ali et al. (2002) using an assay with suspended actin. This difference is likely to be caused by the geometry of the polTIRF system, in which actin is fixed to the surface, preventing myoV from stepping all the way around the actin filament and thereby altering the number of sideways steps.

myoV-4IQ, with a truncated lever arm, has a $\Delta\alpha_L$ distribution with a central peak near zero and two shoulders to the left and right, all with means similar to those for the native myoV-6IQ (Fig. 8 and Table 3). However, the two constructs differ significantly in the relative frequencies of these three subpopulations; myoV-4IQ has an approximately equal probability for stepping left, right, or straight for any given single step, whereas myoV-6IQ walks straight more often. These results are consistent with those of the myoV-4IQ gliding filament assays, where most of the observed actin filaments twirled (94%) with a left-handed (56%) or right-handed pitch (38%), a loss of azimuthal bias in the twirling of actin that has not been observed before for any other myosin family member (Sun et al., 2007; Beausang et al., 2008a). In the kinesin family of microtubule motors, a somewhat analogous observation has been made for Ncd, where a point mutation in its neck linker region led to a loss of directional bias in microtubule gliding assays (Endow and Higuchi, 2000). Individual microtubules were driven by this mutant in either the plus- or minus-end direction. Such behavior in the ensemble assay suggests that cooperation between the motors that are linked through the cytoskeletal filament promotes directional concordance of individual motors that have limited directional bias, thereby maintaining an initial directionality. In the case of myoV-4IQ observed here, the axial direction along the actin filament (toward the barbed end) is not variable, but the frequency for an individual motor to step sideways is high, as discussed below, and leftward and rightward steps have similar probabilities. Linking the motors through the filament apparently coordinates this helical direction, leading to either left- or right-handed twirling.

Correlating the azimuth of stepping myoV to the helical structure of F-actin

Subunits of F-actin form a right-handed helix with a helical half-pitch repeat of ~13 subunits that span ~36 nm, the same distance as the average step size of myoV

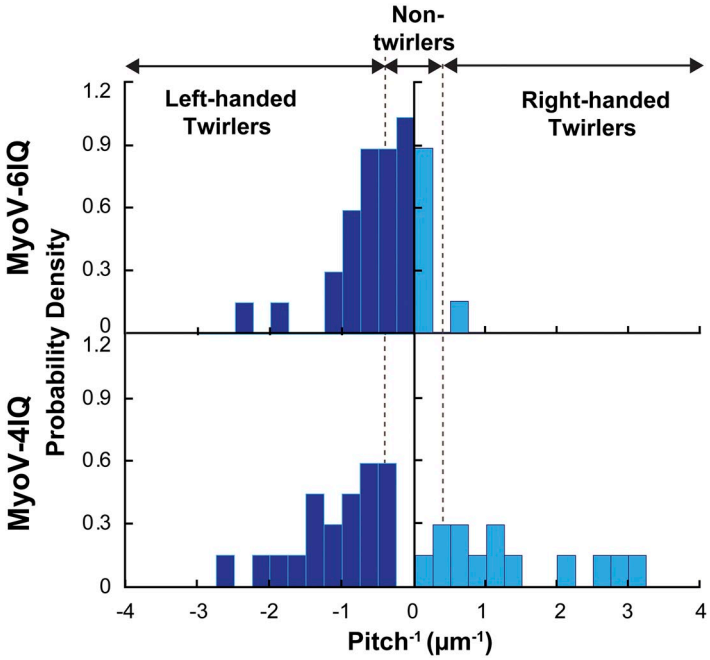

Figure 10. Inverse pitch (μm^{-1}) distributions for myoV-6IQ and myoV-4IQ. Histograms of the inverse pitch (μm^{-1}) calculated from individual actin filaments twirling along either myoV-6IQ (top) or myoV-4IQ (bottom) construct. The histograms are normalized. Actin filaments with an inverse pitch $<\pm 0.4$ μm^{-1} (pitch > 2.5 µm) are classified as non-twirlers. myoV-6IQ twirls with a left-handed pitch, with a mean value of 1.4 µm, whereas myoV-4IQ twirls either with a left- or right-handed pitch, with mean values of 1.2 and 1.0 µm, respectively.

(Mehta et al., 1999). Because both motor domains of myoV bind stereo-specifically to subunits of actin, the azimuthal difference between the two heads of myoV is equal to the difference between the two bound actin subunits. Electron microscopy (EM) studies have shown that a single step of myoV can span 11, 13, or 15 actin subunits (Walker et al., 2000; Oke et al., 2010), corresponding to discrete changes in the myoV azimuth of $\Delta\alpha_L = -28°$, 0°, and +28°, respectively, values reasonably close to the three $\Delta\alpha_L$ subpopulations for native myoV-6IQ ($\Delta\alpha_L$ averaging −29°, −1.8°, and +33°). Thus, the polTIRF measurements indicate that the native myoV-6IQ principally spans 13 actin subunits and less frequently spans 11 or 15 subunits, the same as observed in EM images obtained from stepping myoV (Walker et al., 2000; Oke et al., 2010).

The principal previously reported effect of shortening the lever arm is that it proportionally shortens the step size; in the case of myoV-4IQ, the step size averaged 24 nm (Purcell et al., 2002; Sakamoto et al., 2005). Based on its mean step size alone, myoV-4IQ should span, on average, approximately eight to nine actin subunits, from which we would expect a $\Delta\alpha_L$ distribution with peaks centered at $\Delta\alpha_L = +111°$ and −55°. This expectation is in contrast to our measured $\Delta\alpha_L$ distribution, which contained three subpopulations with peaks at $\Delta\alpha_L = -35°$, −1.4°, and +47°. What is the source of this discrepancy between expectation and observation? The answer to this most likely lies in the broad step-size distribution of myoV-4IQ obtained from optical trap measurements, which Purcell et al. (2002) noted is twice as wide as that of myoV-6IQ, implying that myoV-4IQ spans a larger range of actin subunits than myoV-6IQ. Considering that the step-size distribution measured in the optical trap is well populated for steps ranging from 10 to 40 nm, this corresponds to a potential range of ∼2–13 actin subunit spans for myoV-4IQ. Consistent with this range, the components at $\Delta\alpha_L = -35°$ and −1.4° we report for myoV-4IQ correspond closely to subunit spans of 11 and 13, also consistent with the observations of Oke et al. (2010). In addition, we detected a significant number of steps of myoV-4IQ with a peak of $\Delta\alpha_L = +47°$, which could correspond to 2 (+28°), 4 (+56°), or 15 subunit spans, although a span of 15 subunits is less likely considering the given range of its step sizes (Purcell et al., 2002). Oke et al. (2010) did not observe two and four subunit spans by EM, which may be related to insufficient sampling of particles with distorted structure, as mentioned in their paper.

It is interesting that, despite the broad step-size distribution of myoV-4IQ, it visits actin subunits within a narrow azimuthal range, $\Delta\alpha_L \approx \pm 40°$. This connection between myoV step-size and predicted azimuthal change was addressed in simulations performed by Vilfan (2005a), who examined likely actin-binding sites of myoV with lever arms containing two, four, six, or eight IQ motifs. The model used in this analysis relied on calculating the bending energies of the four myoV constructs. Because of high bending energies in the myoV lever arm associated with large azimuthal changes, all of the constructs were limited to spanning 2, 11, 13, or 15 actin subunits, for which the azimuthal changes fall in the range of $\Delta\alpha_L = \pm 28°$. When Vilfan later included the natural fluctuations in the actin helix, which can vary ±5° in the azimuthal direction (Egelman, 1997), the model then predicted steps up to $\Delta\alpha_L = \pm 56°$ for some of the constructs (Vilfan, 2005b). This model well predicts the observed step sizes for myoV-4IQ and myoV-6IQ, and predicts subunit spans of 2, 4, and 11 for myoV-4IQ, similar to those implied by our $\Delta\alpha_L$ distribution (Fig. 8 B) and the myoV-4IQ step-size distribution (Purcell et al., 2002).

The mean step size (Purcell et al., 2002; Sakamoto et al., 2005) and actin subunit span (Oke et al., 2010) of myoV are clearly dependent on the length of its lever arm. It is therefore surprising that the means of the $\Delta\alpha_L$ distributions, related to the span over actin subunits, are so similar between myoV-6IQ and myoV-4IQ (Fig. 8 and Table 3). Our results on myoV-6IQ and myoV-4IQ, and the Vilfan model, strongly suggest that the azimuthal range of myoV on the actin filament is largely independent of the length of its lever arm. This constraint on its azimuth is likely a result of the relatively high stiffness of the myoV lever arm, probably leading to approximately equal azimuthal stiffness as the actin, which would energetically exclude large bending angles (Vilfan, 2005a; Sun and Goldman, 2011) and may even straighten the actin helix somewhat between the two bound heads. Although the lever arm constrains the azimuthal motions of myoV-4IQ to a range similar to that of myoV-6IQ, the myoV-4IQ construct takes more sideways steps than myoV-6IQ, presumably because its truncated lever arm makes straight steps that necessitate stretching 36 nm, less energetically favorable. We speculate that the consequent extra strain increases the likelihood of stepping sideways. Nevertheless, the range of azimuthal angles is limited by the discrete angles of the actin helix, relatively independent of the neck length. A different isoform, myosin VI, has a much larger range of step sizes and azimuthal positions because its lever arm is very flexible (Sun et al., 2007).

Subpopulations in θ_P versus φ_P distributions may indicate different labeling positions for the BR-CaM

The distribution of θ_P versus φ_P from the processive runs of the myoV-6IQ constructs reveal three fairly distinct subpopulations (Fig. 6 A and Table 4) that quantify the orientation of the probe relative to the lever arm of the individual myoVs that were observed (Fig. 1 A). A crystal structure–based model of the isolated LCD with associated CaMs shows that each CaM has a different binding orientation relative to the heavy chain (Terrak et al., 2005). The three different subpopulations of

(θ_P, φ_P) pairs most likely arise from labeled CaMs binding to different IQ motifs in the lever arm. Strikingly, the three subpopulations of (θ_P, φ_P) in myoV-6IQ are also apparent in the myoV-4IQ distributions with similar peak values (Fig. 6 A and Table 4). Because myoV-4IQ has only the first four IQ motifs in its lever arm (Materials and methods), this similarity in the observed (θ_P, φ_P) pairs suggests that the IQ motifs to which labeled CaMs are bound are limited to sites 1–4 for both constructs. The existence of multiple exchange sites is supported by other single-molecule experiments, also using BR-CaM–labeled myoV, from which they also concluded that their results came from a heterogeneous population of myoVs labeled at different IQ sites (Syed et al., 2006; Toprak et al., 2006).

We can more closely identify the IQ sites that likely correspond to our data by using a recently constructed molecular mechanical model of a myoV dimer with the two motor domains bound to actin 13 subunits apart (Parker et al., 2009). From this model, we calculated the parameters θ_P, φ_P, β_P, α_P, β_L, and α_L for each of the six CaMs in both its leading and trailing positions (Table S5 and Fig. S11). The probe orientation was taken from a vector drawn between the β-carbon atoms of the two amino acids in CaM replaced with cysteines and labeled with BR (P66 and A73) (Corrie et al., 1998; Forkey et al., 2003); the lever-arm orientation was taken from a vector tangent to the myosin heavy chain near the center of each IQ motif. The probe orientations corresponding to the first three IQ positions have values for (θ_P, φ_P) that are similar to the centers of the subpopulations from the (θ_P, φ_P) distributions for myoV-6IQ and myoV-4IQ (Tables 4 and S5, and Fig. S11), whereas CaM positions 4–6 differ substantially from the measured (θ_P, φ_P) values. This suggests that the three subpopulations isolated from the θ_P versus φ_P distributions resulted from the labeled CaMs binding to the first, second, and third IQ motifs. The CaM bound to the second IQ motif of myoV has been reported to dissociate most easily in the presence of calcium (Trybus et al., 2007) and so is the most likely one to exchange with BR-CaM in our labeling procedure (Materials and methods). Furthermore, because the second CaM makes contacts with neighboring CaMs, it is possible that its dissociation would destabilize the CaMs bound to the first and third IQ motifs, thus making them targets for exchange with BR-CaM as well.

Evaluating the assumptions in the myoV analysis

Two important assumptions about myoV stepping are required for determining (θ_P, φ_P) in the present analysis. The first assumption is that its lever arms are straight in the double-headed attached state during stepping. Given a myoV with two straight lever arms of the same length, the myosin and actin form an isosceles triangle and $\beta_{L,leading} + \beta_{L,trailing} = 180°$. Previous studies have proposed that the lever arm on the leading head can adopt a "telemark" or kinked configuration (Snyder et al., 2004). However, markedly kinked lever arms are unusual in cryo-EM images (Walker et al., 2000; Oke et al., 2010).

To determine how a curved or kinked lever arm could perturb our analysis, we again turned to the molecular model of myoV (see above and Parker et al., 2009), which has a curved leading lever arm. The sum $\beta_{L,leading} + \beta_{L,trailing}$ from this model can be compared with the 180° value imposed by the analysis. In this model, the probe at IQ position 3 has $\beta_{L,leading} + \beta_{L,trailing} \cong 180°$, and the values for ($\theta_P$, φ_P) closely match the values determined from the third peak of the (θ_P, φ_P) distribution (Table S5 and Fig. S11). $\beta_{L,leading} + \beta_{L,trailing}$ in IQ positions 1 and 2 of the model are 163° and 144°, and the values for (θ_P, φ_P) in peaks 1 and 2 of the experimental θ_P versus φ_P distributions (Table S5 and Fig. S11) are also moderately shifted by 10° and 20°, respectively, from the corresponding model orientations. This difference illustrates that the primary consequence of the assumption of straight lever arms is a possible small deviation of θ_P and φ_P related to the degree of curvature of the lever arm.

The second assumption made in the analysis is that there is no azimuthal twist (γ) of the lever arm around its own axis relative to the motor domain. γ and φ_P sum together in all coordinate calculations, so as long as γ is constant, its value is equivalent to setting an offset for φ_P without loss of generality. If γ is variable, then calculated φ_P would be offset from its true value. Some of the offsets observed between the myoV model and our data (Fig. S11 and Table S5) may be accounted for by twist in the lever arm between the leading and trailing positions.

Extending the analysis for myoV to other systems

The analysis described here can be applied to other biological molecules, particularly molecular motors, rotary energy convertors, and nucleic acid–processing enzymes. Many enzymes and macromolecules undergo rotational motions as part of their functional mechanisms. For the detailed analysis described here to work, some of the features of molecular motor stepping should apply, including discrete orientations that are repeated in successive enzymatic cycles, a fixed or detectable rotational frame of reference, and labeling methodology that fixes a probe dipole relative to a domain that undergoes functionally relevant rotations. Other myosins, kinesins, or dyneins that walk along filaments with a hand-over-hand mechanism could use the analysis presented in this paper with little modification. The assumptions used in the analysis (straight lever arm and constant local twist angle) would need to be valid. In other myosins and in kinesins, the structure of the waiting state between steps and the dynamic changes during steps are not defined well (Block, 2007; Sweeney and Houdusse, 2010). With dynein, the basic motion of the step or stroke is not

understood well, such as whether its AAA^+ ring rotates during a step (Numata et al., 2008; Gennerich and Vale, 2009). These applications of detailed polTIRF analysis are relatively straightforward. When the local orientation of the probe (θ_P, φ_P) is already known (i.e., from a crystal structure), the assumption that the labeled domain is straight could be relaxed. This was not done for myoV because its 12 potential labeling positions have different φ_P angles.

AAA^+ ring proteins, besides dynein, constitute a large family of macromolecular machines requiring functionally important rotational motions. In the mitochondrial F1 ATP synthase, the coupling between the hydrolysis or reformation of ATP and tilting of the subunits is described by several different models (Nakanishi-Matsui et al., 2010; Okuno et al., 2011) that might be distinguished using polTIRF. Similarly, the coupling between ATPase activity of viral portal motors and pumping of DNA into the viral capsid is not settled (Moffitt et al., 2009).

The ribosome and ribosomal elongation factors undergo rotational motions, but the relationship between these motions to proofreading of aminoacyl-tRNA selection and to translocation of the messenger RNA are unknown (Schmeing and Ramakrishnan, 2009). DNA- and RNA-processing enzymes are natural applications of orientational analysis resulting from the helical nature of duplex nucleic acids. Topoisomerases and helicases exhibit large rotational motions, whose coupling to topological adjustments of the DNA and to unwinding of secondary structure is uncertain (Bustamante et al., 2011; Klostermeier, 2011). In all of these cases, details of the structural dynamics in real time may be determined and correlated with the functional outputs by analyzing polTIRF recordings as we have done for myoV.

Conclusions

We found that the removal of two IQ motifs from the LCD of myoV led to myoV-4IQ taking fewer straight steps than the native myoV-6IQ construct, as we expected. However, considering the 24-nm step size of myoV-4IQ, the observation that the myoV-4IQ and myoV-6IQ took steps to the left and right with similar magnitude but different frequencies, as measured by $\Delta\alpha_L$, was unexpected. These findings suggest that the step-wise changes in the azimuth of myoV are limited by the stiffness of its lever arm to $\Delta\alpha_L = \pm 28°$ and their frequency is determined by the length of the lever arm. We also found three distinct subpopulations in the distribution of the (θ_P, φ_P) angles (Figs. 6 A and S9). We tentatively attribute these subpopulations to distinct binding sites of the labeled BR-CaM on the lever arm of myoV. This conclusion supports other studies that have also inferred BR-CaM binding to three separate sites on the LCD (Syed et al., 2006; Toprak et al., 2006). The (θ_P, φ_P) values calculated from our polTIRF data also roughly agree with values predicted for the IQ positions 1, 2, and 3 from a molecular model of myoV (Parker et al., 2009). The analysis that we developed to transform the measured probe angles to the more functionally relevant lever angles is sufficiently general to be applied to other proteins, with repeating conformational changes measured using polTIRF.

APPENDIX

1. Derivation of expression for the orientation of the probe relative to actin (α_P, β_P) as a function of the lever-arm orientation (α_L, β_L) and probe orientation relative to the lever-arm frame (θ_P, φ_P)

The intensities measured in our experiments are used to calculate the orientation of the probe attached to myoV relative to the laboratory frame of reference ($\theta_{laboratory}$, $\varphi_{laboratory}$), which we then transform to the actin reference frame (α_P, β_P). The orientation of the probe can also be described relative to the frame of the lever-arm (θ_P, φ_P), whose orientation is itself expressed relative to the actin frame (α_L, β_L) (Fig. 1 A and Materials and methods).

In deriving an expression relating the orientations of the probe to the lever arm in the actin frame, we note that this expression must also account for the orientation of the probe relative to the frame of the lever arm. We construct the rotation matrix ${}^A\mathbf{R}^P$, which is derived from four separate rotation operations that rotate the probe frame (P) to the actin frame (A) (Fig. S2). The combined rotation matrix ${}^A\mathbf{R}^P$ is derived by multiplying together the four rotation matrices. We describe rotations as changes in the angles β_L, α_L, θ_P, and φ_P. The first two rotations that align the z_A axis with the lever arm are performed so that the resulting axes are consistent with our definition of the lever-arm frame of reference (Fig. 1 A and Materials and methods).These initial rotations are performed on the actin frame of reference, defined by the axes x_0, y_0, and z_0 (where $x_0 = x_A$, $y_0 = y_A$, and $z_0 = z_A$; Fig. S2 A). The first rotation matrix describes the rotation of these axes about the z_0 axis by an amount equal to $(\pi/2 - \alpha_L)$, so that the y_0 axis is aligned with the projection of the lever arm that lies in the x_0–y_0 plane perpendicular to the actin filament:

$$ {}^0\mathbf{R}^1 = Rot\left(z_0, -\left(\frac{\pi}{2} - \alpha_L\right)\right) = \begin{bmatrix} \sin\alpha_L & \cos\alpha_L & 0 \\ -\cos\alpha_L & \sin\alpha_L & 0 \\ 0 & 0 & 1 \end{bmatrix}. \quad (A.1) $$

This rotation results in a coordinate frame defined by x_1, y_1, and z_1, where $z_1 = z_0$ (Fig. S2 B). The second rotation matrix describes the rotation about the x_1 axis by an amount equal to β_L, so that the z_1 axis is aligned with the lever vector:

$$ {}^1\mathbf{R}^2 = Rot\left(x_1, -\beta_L\right) = \begin{bmatrix} 1 & 0 & 0 \\ 0 & \cos\beta_L & \sin\beta_L \\ 0 & -\sin\beta_L & \cos\beta_L \end{bmatrix}. \quad (A.2) $$

This rotation results in a coordinate frame defined by x_2, y_2, and z_2, where $x_2 = x_1 = x_L$, $y_2 = y_L$, and $z_2 = z_L$, where the x_L, y_L, and z_L axes describe the lever-arm frame of reference (Figs. S2, B and C). The third rotation matrix describes the rotation about the z_2 axis by an amount equal to $(\pi/2 - \varphi_P)$, so that the y_2 axis is aligned with the projection of the probe that lies in the x_3–y_3 plane perpendicular to the lever arm:

$$ {}^{2}\mathbf{R}^{3} = Rot\left(z_2, -\left(\frac{\pi}{2} - \varphi_P\right)\right) = \begin{bmatrix} \sin\varphi_P & \cos\varphi_P & 0 \\ -\cos\varphi_P & \sin\varphi_P & 0 \\ 0 & 0 & 1 \end{bmatrix}. \quad (A.3) $$

This rotation results in a coordinate frame defined by x_3, y_3, and z_3, where $z_3 = z_2$ (Fig. S2 D). The final rotation matrix describes the rotation about the x_3 axis by an amount equal to θ_P, so that the z_3 axis is aligned with the probe vector:

$$ {}^{3}\mathbf{R}^{4} = Rot\left(x_3, -\theta_P\right) = \begin{bmatrix} 1 & 0 & 0 \\ 0 & \cos\theta_P & \sin\theta_P \\ 0 & -\sin\theta_P & \cos\theta_P \end{bmatrix}. \quad (A.4) $$

The total rotation operation is described by:

$$ {}^{A}\mathbf{R}^{P} = {}^{0}\mathbf{R}^{4} = {}^{0}\mathbf{R}^{1} \cdot {}^{1}\mathbf{R}^{2} \cdot {}^{2}\mathbf{R}^{3} \cdot {}^{3}\mathbf{R}^{4}. \quad (A.5) $$

The result of this last rotational operation is that the z_3 axis is aligned with the vector of the probe $\vec{\mathbf{v}}_P$ (Fig. S2 E), where the $x_4 = x_P$, $y_4 = y_P$, and $z_4 = z_P$ axes represent a probe frame of reference. In the probe frame, $\vec{\mathbf{v}}_P$ is a unit vector aligned with the z_4 axis:

$$ \vec{\mathbf{v}}_P = \begin{pmatrix} v_{P,x} \\ v_{P,y} \\ v_{P,z} \end{pmatrix} = \begin{pmatrix} 0 \\ 0 \\ 1 \end{pmatrix}. \quad (A.6) $$

$\vec{\mathbf{v}}_P$ is a vector defined in the probe frame (P) and can be redefined in the actin frame (A) as the vector $\vec{\mathbf{v}}_A$:

$$ \begin{pmatrix} v_{A,x} \\ v_{A,y} \\ v_{A,z} \end{pmatrix} = \vec{\mathbf{v}}_A = {}^{A}\mathbf{R}^{P} \cdot \vec{\mathbf{v}}_P. \quad (A.7) $$

This is converted to α_P and β_P using the following trigonometric relationships:

$$ \alpha_P = \mathrm{atan2}\left(v_{A,x}, v_{A,y}\right) \quad (A.8) $$

$$ \beta_P = \mathrm{acos}\left(v_{A,z}\right) \quad (A.9) $$

Solving the above relationships, we find the two expressions for α_P and β_P as functions of α_L, β_L, θ_P, and φ_P:

$$ \beta_P\left(\theta_P, \varphi_P, \beta_L\right) = \mathrm{acos}\left(-\sin\beta_L \cdot \sin\theta_P \cdot \sin\varphi_P + \cos\beta_L \cdot \cos\theta_P\right), \quad (A.10) $$

where:

$$ 0 \le \beta_P \le \pi \quad (A.11) $$

$$ \alpha_P\left(\theta_P, \varphi_P, \alpha_L, \beta_L\right) = \mathrm{atan2}(v_{A,x}, v_{A,y}), \quad (A.12) $$

where expressions for $v_{A,x}$ and $v_{A,y}$ are given in the main text Eq. 1, and:

$$ -\pi \le \alpha_P \le \pi \quad (A.13) $$

and the atan2(x, y) function is similar to the standard arctan(y/x) function, except that atan2(x, y) is single valued over a larger range ($-\pi \le \alpha_P \le \pi$ vs. $-\pi/2 \le \alpha_P \le \pi/2$ for arctan(y/x)).

2. Derivation of expression for lever-arm orientation relative to actin (α_L, β_L) as a function of the probe orientation relative to actin (α_P, β_P) and relative to the lever-arm (θ_P, φ_P)

We wish to find an expression for the orientation of the lever arm in terms of the orientation of the probe, both in relation to the actin frame of reference (x_A, y_A, z_A). We start by rearranging Eq. A.10:

$$ -\sin\beta_L \cdot \sin\theta_P \cdot \sin\varphi_P = \cos\beta_L \cdot \cos\theta_P - \cos\beta_P \quad (A.14) $$

$$ \left(-\sin\beta_L \cdot \sin\theta_P \cdot \sin\varphi_P\right)^2 = \left(\cos\beta_L \cdot \cos\theta_P - \cos\beta_P\right)^2 \quad (A.15) $$

$$ \left(1 - \cos\beta_L^{\,2}\right) \cdot \sin\theta_P^{\,2} \cdot \sin\varphi_P^{\,2} = \cos\beta_L^{\,2} \cdot \cos\theta_P^{\,2} + \cos\beta_P^{\,2} - 2 \cdot \left(\cos\beta_L \cdot \cos\theta_P \cdot \cos\beta_P\right) \quad (A.16) $$

$$ \cos\beta_L^{\,2} \cdot \left(\cos\theta_P^{\,2} + \sin\theta_P^{\,2} \cdot \sin\varphi_P^{\,2}\right) - \cos\beta_L \cdot \left(2 \cdot \cos\theta_P \cdot \cos\beta_P\right) + \left(\cos\beta_P^{\,2} - \sin\theta_P^{\,2} \cdot \sin\varphi_P^{\,2}\right) = 0 \quad (A.17) $$

We then find an expression for β_L:

$$ \beta_L\left(\theta_P, \varphi_P, \beta_P\right) = \mathrm{acos}\left(\frac{\cos\theta_P \cdot \cos\beta_P \pm \sqrt{\sin\theta_P^{\,2} \cdot \sin\varphi_P^{\,2} \cdot \left(\sin\beta_P^{\,2} - \sin\theta_P^{\,2} \cdot \cos\varphi_P^{\,2}\right)}}{\cos\theta_P^{\,2} + \sin\theta_P^{\,2} \cdot \sin\varphi_P^{\,2}}\right), \quad (A.18) $$

where:

$$ 0 \le \beta_L \le \pi. \quad (A.19) $$

To solve for α_L, we rearrange Eq. A.12:

$$\tan\alpha_P = \frac{\left(-\cos\varphi_P + \tan\alpha_L \cdot \cos\beta_L \cdot \sin\varphi_P\right)\cdot \sin\theta_P + \tan\alpha_L \cdot \sin\beta_L \cdot \cos\theta_P}{\left(\tan\alpha_L \cdot \cos\varphi_P + \cos\beta_L \cdot \sin\varphi_P\right)\cdot \sin\theta_P + \sin\beta_L \cdot \cos\theta_P}. \tag{A.20}$$

$$\begin{aligned}&\tan\alpha_L \cdot \left(\sin\theta_P \cdot \tan\alpha_P \cdot \cos\varphi_P - \sin\theta_P \cdot \cos\beta_L \cdot \sin\varphi_P - \sin\beta_L \cdot \cos\theta_P\right)\\ &= \tan\alpha_P \cdot \left(\sin\theta_P \cdot \cos\beta_L \cdot \sin\varphi_P + \sin\beta_L \cdot \cos\theta_P\right) - \sin\theta_P \cdot \tan\alpha_P \cdot \cos\varphi_P\end{aligned} \tag{A.21}$$

Rearranging this yields an expression for

$$\alpha_L\left(\theta_P, \varphi_P, \alpha_P, \beta_P\right) = \operatorname{atan2}(w_{A,x}, w_{A,y}), \tag{A.22}$$

where expressions for $w_{A,x}$ and $w_{A,y}$ are given in the main text Eq. 3, where:

$$-\pi \le \alpha_L \le \pi. \tag{A.23}$$

3. Equality between ${}^m\Delta\alpha_P$ and ${}^m\Delta\alpha_L$ when m is even

We consider the difference in orientation of the probe between two angular states:

$${}^m\Delta\beta_n = \beta_{n+m} - \beta_n \tag{A.24}$$

$${}^m\Delta\alpha_n = \alpha_{n+m} - \alpha_n, \tag{A.25}$$

where:

$$n = 1, 2 \ldots N - m \tag{A.26}$$

$$m = 1, 2 \ldots N - n. \tag{A.27}$$

Note that m denotes the number of the intervals in the difference ${}^m\Delta$ and is even when two leading or two trailing states of myoV are considered. Given the conditions of our model for myoV, where θ_P and φ_P are constant over all n and m and the lever arms are straight (Materials and methods), when m is even:

$$\beta_{P,n} = \beta_{P,n+m}. \tag{A.28}$$

Under the conditions given above, and when m is even, the trigonometric identity

$$\tan\left(A - B\right) = \left(\frac{\tan A - \tan B}{1 + \tan A \cdot \tan B}\right) \tag{A.29}$$

is applied to a modified Eq. A.25:

$$\tan\left({}^m\Delta\alpha_{P,n}\right) = \tan\left(\alpha_{P,n+m} - \alpha_{P,n}\right), \tag{A.30}$$

and Eq. A.12, simplifying to:

$$\tan\left(\alpha_{P,n+m} - \alpha_{P,n}\right) = \frac{\tan\alpha_{L,n+m} \cdot \sec^2\alpha_{L,n} - \tan\alpha_{L,n} \cdot \sec^2\alpha_{L,n+m}}{1 - \tan^2\alpha_{L,n} \cdot \tan^2\alpha_{L,n+m}}. \tag{A.31}$$

Using the trigonometric identity

$$\sec^2 A = 1 + \tan^2 A, \tag{A.32}$$

Eq. A.31 simplifies to:

$$\tan\left(\alpha_{P,n+m} - \alpha_{P,n}\right) = \frac{\tan\alpha_{L,n+m} - \tan\alpha_{L,n}}{1 + \tan\alpha_{L,n} \cdot \tan\alpha_{L,n+m}}. \tag{A.33}$$

Using the identity given in Eq. A.29, we find that:

$$\tan\left(\alpha_{P,n+m} - \alpha_{P,n}\right) = \tan\left(\alpha_{L,n+m} - \alpha_{L,n}\right), \tag{A.34}$$

which is equivalent to:

$$\alpha_{P,n+m} - \alpha_{P,n} = \alpha_{L,n+m} - \alpha_{L,n} \tag{A.35}$$

when the tan function is single valued; i.e.:

$$-\frac{\pi}{2} \le \left(\alpha_{n+m} - \alpha_n\right) \le \frac{\pi}{2}. \tag{A.36}$$

We complete the derivation by noting that using Eq. A.25, Eq. A.35 can be identically expressed as:

$${}^m\Delta\alpha_P = {}^m\Delta\alpha_L \tag{A.37}$$

when m is even.

4. Reconstructing the relative α_L path using the relationship ${}^2\Delta\alpha_P = {}^2\Delta\alpha_L$

We consider Eq. A.37, under the conditions given in Section 3 of this Appendix, when $m = 2$:

$${}^2\Delta\alpha_{P,n} = {}^2\Delta\alpha_{L,n}. \tag{A.38}$$

When $m = 1$, Eq. A.25 can be expressed as:

$${}^1\Delta\alpha_n = \alpha_{n+1} - \alpha_n = \Delta\alpha_n, \tag{A.39}$$

and when $m = 2$, Eq. A.25 is:

$${}^2\Delta\alpha_n = \alpha_{n+2} - \alpha_n = (\alpha_{n+1} - \alpha_n) + (\alpha_{n+2} - \alpha_{n+1}) = \Delta\alpha_n + \Delta\alpha_{n+1}. \tag{A.40}$$

In general, the difference between two angular states separated by m intervals can be expressed as:

$$ {}^{m}\Delta_n = \Delta_n + \Delta_{n+1} + \cdots + \Delta_{n+(m-1)} = \sum_{i=1}^{m-1} \Delta_{n+i} \tag{A.41} $$

over all values of m and n. Using Eq. A.41, Eq. A.38 is then expressed as:

$$ \Delta\alpha_{P,n} + \Delta\alpha_{P,n+1} = \Delta\alpha_{L,n} + \Delta\alpha_{L,n+1}, \tag{A.42} $$

which is rearranged to define a factor, R, which expresses the effect of the probe orientation out of the plane of lever-arm rotation on $\Delta\alpha_P$ and is constant over all n:

$$ \begin{aligned} &\Delta\alpha_{P,n} - \Delta\alpha_{L,n} = \Delta\alpha_{L,n+1} - \Delta\alpha_{P,n+1} \\ &= (-1)^{m-1} \cdot \left(\Delta\alpha_{P,n+(m-1)} - \Delta\alpha_{L,n+(m-1)}\right) \equiv R. \end{aligned} \tag{A.43} $$

This allows us to express $\Delta\alpha_P$ as the sum of $\Delta\alpha_L$ and R:

$$ \Delta\alpha_{P,n} = (-1)^n \cdot R + \Delta\alpha_{L,n}. \tag{A.44} $$

Therefore, calculating $\Delta\alpha_L$ from $\Delta\alpha_P$ depends on finding a reliable value for R. We take the average of our measured values of $\Delta\alpha_P$ over all n:

$$ \overline{\Delta\alpha_P} = \frac{1}{N-1} \cdot \left(\sum_{n=1}^{N-1} (-1)^n \cdot \Delta\alpha_{P,n}\right). \tag{A.45} $$

Using Eq. A.44, this is then expressed as:

$$ \begin{aligned} \overline{\Delta\alpha_P} &= \frac{1}{N-1} \cdot \sum_{n=1}^{N-1} \left((-1)^n \cdot \Delta\alpha_{P,n} + R\right) \\ &= R + \frac{1}{N-1} \cdot \sum_{n=1}^{N-1} \left((-1)^n \cdot \Delta\alpha_{P,n}\right). \end{aligned} \tag{A.46} $$

From this relation we find that:

$$ \overline{\Delta\alpha_P} = R \tag{A.47} $$

is true for all values of n and m when:

$$ \Delta\alpha_{L,n} = \Delta\alpha_{L,n+m}, \tag{A.48} $$

and the maximum value of $n = N - 1$ is even, where N is the total number of angular states.

We then extend this to the general case in which Eq. A.48 does not hold. Because of this, the mean of these $\Delta\alpha_P$s does not necessarily equate to R as in the simple case detailed above. If we assume for a given run of myoV that Eq. A.48 is true for some of the $\Delta\alpha_{L,n}$s because there is a predominant azimuthal motion upon each step, we can calculate R by taking a weighted average of all of the $\Delta\alpha_{P,n}$ values. A weighted average excludes values of $\Delta\alpha_{P,n}$ that significantly deviate from the average $\Delta\alpha_P$. The weighting function, W, is defined by:

$$ W_n = \frac{1}{\left(\left|\Delta\alpha_{P,n} - \overline{\Delta\alpha_P}\right| + \varepsilon\right)^r}, \tag{A.49} $$

where $\Delta\alpha_{P,n}$ is defined in Eq. A.44, and $\overline{\Delta\alpha_P}$ is the unweighted average. In addition, a small value, ε, is chosen to avoid division by 0, and r is an even positive integer. A value near zero is added to the residual in the weighting function to prevent division by 0. The weighting function is then applied by combining Eq. A.45 with Eq. A.49 to give:

$$ \overline{\Delta\alpha_P} = \frac{\sum_{n=1}^{N-1} (-1)^n \cdot W_n \cdot \Delta\alpha_{P,n}}{\sum_{n=1}^{N-1} W_n}. \tag{A.50} $$

Because the weighting function excludes values of $\Delta\alpha_{P,n}$ that significantly deviate from the mean $\overline{\Delta\alpha_P}$, and hence values of $\Delta\alpha_{L,n}$ that are significantly different from the mean $\overline{\Delta\alpha_L}$ (for instance, when a relatively straight-walking molecule takes a sudden sideways step), Eq. A.48 is largely satisfied, and:

$$ \overline{\Delta\alpha_{P\ weighted}} \cong R. \tag{A.51} $$

Eq. A.50 therefore allows us to calculate a reasonable value for R, even in the more general case where Eq. A.48 does not hold for all n, as long as there are a significant number of $\Delta\alpha_{L,n}$s for which it is true (e.g., the molecule either walks relatively straight [$\Delta\alpha_{L,n} = 0$], or it has a typical azimuthal motion [$\Delta\alpha_{L,n} \cong \overline{\Delta\alpha_L}$]).

5. Rationale for calculating the orientation of the probe relative to the lever-arm (θ_P, φ_P) for individual processive runs

We again consider the probe at two angular states, n and $n + m$ (Eqs. A.24–A.27), in the case where the condition for β_P given in Eq. A.28 is satisfied. Solutions for α_L and β_L are defined over all θ_P–φ_P space as:

$$ \alpha_{L,n} = \alpha_L\left(\theta_P, \varphi_P, \alpha_{P,n}, \beta_{P,n}\right) \tag{A.52} $$

$$ \beta_{L,n} = \beta_L\left(\theta_P, \varphi_P, \beta_{P,n}\right) \tag{A.53} $$

We first consider the general case where:

$$ \alpha_{L,n+m} - \alpha_{L,n} = \Delta\alpha_{L,n} \tag{A.54} $$

$$ \alpha_L\left(\theta_P, \varphi_P, \alpha_{P,n}, \beta_{P,n}\right) - \alpha_L\left(\theta_P, \varphi_P, \alpha_{P,n+m}, \beta_{P,n+m}\right) = \Delta\alpha_{L,n} \tag{A.55} $$

$$ \beta_{L,n} + \beta_{L,n+m} = {}^{Tot}\beta_{L,n} \tag{A.56} $$

$$ \beta_L\left(\theta_P, \varphi_P, \beta_{P,n}\right) + \beta_L\left(\theta_P, \varphi_P, \beta_{P,n+m}\right) = {}^{Tot}\beta_{L,n}, \tag{A.57} $$

where m is nonzero and odd.

We then look at the specific case where $m = 1$, ${}^{Tot}\beta_L = \pi$, and $\Delta\alpha_L = 0$:

$$\alpha_L\left(\theta_P, \varphi_P, \alpha_{P,n}, \beta_{P,n}\right) - \alpha_L\left(\theta_P, \varphi_P, \alpha_{P,n+1}, \beta_{P,n+1}\right) = 0 \quad \text{(A.58)}$$

$$\beta_L\left(\theta_P, \varphi_P, \beta_{P,n}\right) + \beta_L\left(\theta_P, \varphi_P, \beta_{P,n+1}\right) = \pi \quad \text{(A.59)}$$

Eqs. A.58 and A.59 represent a system of two equations that share the six parameters θ_P, φ_P, $\beta_{P,n}$, $\beta_{P,n+1}$, $\alpha_{P,n}$, and $\alpha_{P,n+1}$. Given our measured values for $\beta_{P,n}$, $\beta_{P,n+1}$, $\alpha_{P,n}$, and $\alpha_{P,n+1}$, the values for the parameters θ_P and φ_P can be solved exactly, assuming a real solution exists, which is addressed below. We can also substitute $\Delta\alpha_{L,n}$ with the values estimated using Eq. A.44 because the conditions under which this equation is used must also be met when calculating θ_P and φ_P. Because we do not have any way to directly estimate ${}^{Tot}\beta_{L,n}$, for this modified general case we use the assumption ${}^{Tot}\beta_{L,n} = 180°$ (corresponding to the situation where both lever arms are straight), as discussed in Materials and methods. This expression is already represented in Eq. A.59.

For a given set of β_P and α_P angles, a range of values of θ_P ($0 \le \theta_P \le \pi$) and φ_P ($-\pi \le \varphi_P \le \pi$) were input into modified versions of Eqs. A.55 and A.59:

$$\left(\alpha_L\left(\theta_P, \varphi_P, \alpha_{P,n}, \beta_{P,n}\right) - \alpha_L\left(\theta_P, \varphi_P, \alpha_{P,n+m}, \beta_{P,n+m}\right)\right) - \Delta\alpha_{L,n} = 0 \quad \text{(A.60)}$$

$$\left(\beta_L\left(\theta_P, \varphi_P, \beta_{P,n}\right) + \beta_L\left(\theta_P, \varphi_P, \beta_{P,n+1}\right)\right) - \pi = 0 \quad \text{(A.61)}$$

Optimum values for θ_P and φ_P corresponded to minima in plots of θ_P and φ_P against the values calculated from Eqs. A.60 and A.61. Over the range of θ_P and φ_P, two such minima would appear, as expected (Materials and methods); one set of θ_P and φ_P is then selected to calculate β_L and α_L using Eqs. A.18 and A.22.

We thank Dr. Robert Dale for useful comments on the manuscript. and Drs. Zev Bryant and David Parker for coordinates of an actomyosin-V model.

This work was supported by National Institutes of Health grant R01GM086352.

Richard L. Moss served as editor.

Submitted: 6 September 2011
Accepted: 21 December 2011

REFERENCES

Ali, M.Y., S. Uemura, K. Adachi, H. Itoh, K. Kinosita Jr., and S. Ishiwata. 2002. Myosin V is a left-handed spiral motor on the right-handed actin helix. *Nat. Struct. Biol.* 9:464–467. http://dx.doi.org/10.1038/nsb803

Ali, M.Y., E.B. Krementsova, G.G. Kennedy, R. Mahaffy, T.D. Pollard, K.M. Trybus, and D.M. Warshaw. 2007. Myosin Va maneuvers through actin intersections and diffuses along microtubules. *Proc. Natl. Acad. Sci. USA.* 104:4332–4336. http://dx.doi.org/10.1073/pnas.0611471104

Amos, L.A., and W.B. Amos. 1991. Molecules of the Cytoskeleton. Guilford Press. 253 pp.

Beausang, J.F., H.W. Schroeder III, P.C. Nelson, and Y.E. Goldman. 2008a. Twirling of actin by myosins II and V observed via polarized TIRF in a modified gliding assay. *Biophys. J.* 95:5820–5831. http://dx.doi.org/10.1529/biophysj.108.140319

Beausang, J.F., Y. Sun, and Y.E. Goldman. 2008b. Single molecule fluorescence polarization via polarized total internal reflection fluorescent microscopy. *In* Laboratory Manual for Single Molecule Studies. P.R. Selvin and T.J. Ha, editors. Cold Spring Harbor Laboratory Press, Cold Spring Harbor, NY. 121–148.

Block, S.M. 2007. Kinesin motor mechanics: binding, stepping, tracking, gating, and limping. *Biophys. J.* 92:2986–2995. http://dx.doi.org/10.1529/biophysj.106.100677

Bustamante, C., W. Cheng, and Y.X. Mejia. 2011. Revisiting the central dogma one molecule at a time. *Cell.* 144:480–497. http://dx.doi.org/10.1016/j.cell.2011.01.033

Cheney, R.E., M.K. O'Shea, J.E. Heuser, M.V. Coelho, J.S. Wolenski, E.M. Espreafico, P. Forscher, R.E. Larson, and M.S. Mooseker. 1993. Brain myosin-V is a two-headed unconventional myosin with motor activity. *Cell.* 75:13–23.

Cooke, R. 1986. The mechanism of muscle contraction. *CRC Crit. Rev. Biochem.* 21:53–118. http://dx.doi.org/10.3109/10409238609113609

Corrie, J.E., and J.S. Craik. 1994. Synthesis and characterization of iodacetamidotetramethylrhodamine. *J. Chem. Soc. Perkin Trans.*1: 2967–2973. http://dx.doi.org/10.1039/p19940002967

Corrie, J.E., J.S. Craik, and V.R. Munasinghe. 1998. A homobifunctional rhodamine for labeling proteins with defined orientations of a fluorophore. *Bioconjug. Chem.* 9:160–167. http://dx.doi.org/10.1021/bc970174e

Corrie, J.E., B.D. Brandmeier, R.E. Ferguson, D.R. Trentham, J. Kendrick-Jones, S.C. Hopkins, U.A. van der Heide, Y.E. Goldman, C. Sabido-David, R.E. Dale, et al. 1999. Dynamic measurement of myosin light-chain-domain tilt and twist in muscle contraction. *Nature.* 400:425–430. http://dx.doi.org/10.1038/22704

Dobbie, I., M. Linari, G. Piazzesi, M. Reconditi, N. Koubassova, M.A. Ferenczi, V. Lombardi, and M. Irving. 1998. Elastic bending and active tilting of myosin heads during muscle contraction. *Nature.* 396:383–387. http://dx.doi.org/10.1038/24647

Egelman, E.H. 1997. New angles on actin dynamics. *Structure.* 5:1135–1137. http://dx.doi.org/10.1016/S0969-2126(97)00264-5

Endow, S.A., and H. Higuchi. 2000. A mutant of the motor protein kinesin that moves in both directions on microtubules. *Nature.* 406:913–916. http://dx.doi.org/10.1038/35022617

Forkey, J.N., M.E. Quinlan, and Y.E. Goldman. 2000. Protein structural dynamics by single-molecule fluorescence polarization. *Prog. Biophys. Mol. Biol.* 74:1–35. http://dx.doi.org/10.1016/S0079-6107(00)00015-8

Forkey, J.N., M.E. Quinlan, M.A. Shaw, J.E. Corrie, and Y.E. Goldman. 2003. Three-dimensional structural dynamics of myosin V by single-molecule fluorescence polarization. *Nature.* 422:399–404. http://dx.doi.org/10.1038/nature01529

Forkey, J.N., M.E. Quinlan, and Y.E. Goldman. 2005. Measurement of single macromolecule orientation by total internal reflection fluorescence polarization microscopy. *Biophys. J.* 89:1261–1271. http://dx.doi.org/10.1529/biophysj.104.053470

Gennerich, A., and R.D. Vale. 2009. Walking the walk: how kinesin and dynein coordinate their steps. *Curr. Opin. Cell Biol.* 21:59–67. http://dx.doi.org/10.1016/j.ceb.2008.12.002

Hecht, E. 2001. Optics. Fourth edition. Addison Wesley, New York. 680 pp.

Klostermeier, D. 2011. Single-molecule FRET reveals nucleotide-driven conformational changes in molecular machines and their

link to RNA unwinding and DNA supercoiling. *Biochem. Soc. Trans.* 39:611–616. http://dx.doi.org/10.1042/BST0390611

Kodera, N., D. Yamamoto, R. Ishikawa, and T. Ando. 2010. Video imaging of walking myosin V by high-speed atomic force microscopy. *Nature.* 468:72–76. http://dx.doi.org/10.1038/nature09450

Mehta, A.D., R.S. Rock, M. Rief, J.A. Spudich, M.S. Mooseker, and R.E. Cheney. 1999. Myosin-V is a processive actin-based motor. *Nature.* 400:590–593. http://dx.doi.org/10.1038/23072

Moffitt, J.R., Y.R. Chemla, K. Aathavan, S. Grimes, P.J. Jardine, D.L. Anderson, and C. Bustamante. 2009. Intersubunit coordination in a homomeric ring ATPase. *Nature.* 457:446–450. http://dx.doi.org/10.1038/nature07637

Nakanishi-Matsui, M., M. Sekiya, R.K. Nakamoto, and M. Futai. 2010. The mechanism of rotating proton pumping ATPases. *Biochim. Biophys. Acta.* 1797:1343–1352. http://dx.doi.org/10.1016/j.bbabio.2010.02.014

Numata, N., T. Kon, T. Shima, K. Imamula, T. Mogami, R. Ohkura, K. Sutoh, and K. Sutoh. 2008. Molecular mechanism of force generation by dynein, a molecular motor belonging to the AAA+ family. *Biochem. Soc. Trans.* 36:131–135. http://dx.doi.org/10.1042/BST0360131

Oke, O.A., S.A. Burgess, E. Forgacs, P.J. Knight, T. Sakamoto, J.R. Sellers, H. White, and J. Trinick. 2010. Influence of lever structure on myosin 5a walking. *Proc. Natl. Acad. Sci. USA.* 107:2509–2514. http://dx.doi.org/10.1073/pnas.0906907107

Okuno, D., R. Iino, and H. Noji. 2011. Rotation and structure of FoF1-ATP synthase. *J. Biochem.* 149:655–664. http://dx.doi.org/10.1093/jb/mvr049

Pardee, J.D., and J.A. Spudich. 1982. Purification of muscle actin. *Methods Cell Biol.* 24:271–289. http://dx.doi.org/10.1016/S0091-679X(08)60661-5

Parker, D., Z. Bryant, and S.L. Delp. 2009. Coarse-grained structural modeling of molecular motors using multibody dynamics. *Cell Mol Bioeng.* 2:366–374. http://dx.doi.org/10.1007/s12195-009-0084-4

Purcell, T.J., C. Morris, J.A. Spudich, and H.L. Sweeney. 2002. Role of the lever arm in the processive stepping of myosin V. *Proc. Natl. Acad. Sci. USA.* 99:14159–14164. http://dx.doi.org/10.1073/pnas.182539599

Putkey, J.A., G.R. Slaughter, and A.R. Means. 1985. Bacterial expression and characterization of proteins derived from the chicken calmodulin cDNA and a calmodulin processed gene. *J. Biol. Chem.* 260:4704–4712.

Reck-Peterson, S.L., D.W. Provance Jr., M.S. Mooseker, and J.A. Mercer. 2000. Class V myosins. *Biochim. Biophys. Acta.* 1496:36–51. http://dx.doi.org/10.1016/S0167-4889(00)00007-0

Rief, M., R.S. Rock, A.D. Mehta, M.S. Mooseker, R.E. Cheney, and J.A. Spudich. 2000. Myosin-V stepping kinetics: a molecular model for processivity. *Proc. Natl. Acad. Sci. USA.* 97:9482–9486. http://dx.doi.org/10.1073/pnas.97.17.9482

Sakamoto, T., I. Amitani, E. Yokota, and T. Ando. 2000. Direct observation of processive movement by individual myosin V molecules. *Biochem. Biophys. Res. Commun.* 272:586–590. http://dx.doi.org/10.1006/bbrc.2000.2819

Sakamoto, T., A. Yildez, P.R. Selvin, and J.R. Sellers. 2005. Step-size is determined by neck length in myosin V. *Biochemistry.* 44:16203–16210. http://dx.doi.org/10.1021/bi0512086

Schmeing, T.M., and V. Ramakrishnan. 2009. What recent ribosome structures have revealed about the mechanism of translation. *Nature.* 461:1234–1242. http://dx.doi.org/10.1038/nature08403

Snyder, G.E., T. Sakamoto, J.A. Hammer III, J.R. Sellers, and P.R. Selvin. 2004. Nanometer localization of single green fluorescent proteins: evidence that myosin V walks hand-over-hand via telemark configuration. *Biophys. J.* 87:1776–1783. http://dx.doi.org/10.1529/biophysj.103.036897

Sun, Y., and Y.E. Goldman. 2011. Lever-arm mechanics of processive myosins. *Biophys. J.* 101:1–11. http://dx.doi.org/10.1016/j.bpj.2011.05.026

Sun, Y., H.W. Schroeder III, J.F. Beausang, K. Homma, M. Ikebe, and Y.E. Goldman. 2007. Myosin VI walks "wiggly" on actin with large and variable tilting. *Mol. Cell.* 28:954–964. http://dx.doi.org/10.1016/j.molcel.2007.10.029

Sweeney, H.L., and A. Houdusse. 2010. Structural and functional insights into the myosin motor mechanism. *Annu Rev Biophys.* 39:539–557. http://dx.doi.org/10.1146/annurev.biophys.050708.133751

Syed, S., G.E. Snyder, C. Franzini-Armstrong, P.R. Selvin, and Y.E. Goldman. 2006. Adaptability of myosin V studied by simultaneous detection of position and orientation. *EMBO J.* 25:1795–1803. http://dx.doi.org/10.1038/sj.emboj.7601060

Terrak, M., G. Rebowski, R.C. Lu, Z. Grabarek, and R. Dominguez. 2005. Structure of the light chain-binding domain of myosin V. *Proc. Natl. Acad. Sci. USA.* 102:12718–12723. http://dx.doi.org/10.1073/pnas.0503899102

Toprak, E., J. Enderlein, S. Syed, S.A. McKinney, R.G. Petschek, T. Ha, Y.E. Goldman, and P.R. Selvin. 2006. Defocused orientation and position imaging (DOPI) of myosin V. *Proc. Natl. Acad. Sci. USA.* 103:6495–6499. http://dx.doi.org/10.1073/pnas.0507134103

Trybus, K.M., M.I. Gushchin, H. Lui, L. Hazelwood, E.B. Krementsova, N. Volkmann, and D. Hanein. 2007. Effect of calcium on calmodulin bound to the IQ motifs of myosin V. *J. Biol. Chem.* 282:23316–23325. http://dx.doi.org/10.1074/jbc.M701636200

Veigel, C., F. Wang, M.L. Bartoo, J.R. Sellers, and J.E. Molloy. 2002. The gated gait of the processive molecular motor, myosin V. *Nat. Cell Biol.* 4:59–65. http://dx.doi.org/10.1038/ncb732

Vilfan, A. 2005a. Elastic lever-arm model for myosin V. *Biophys. J.* 88:3792–3805. http://dx.doi.org/10.1529/biophysj.104.046763

Vilfan, A. 2005b. Influence of fluctuations in actin structure on myosin V step size. *J. Chem. Inf. Model.* 45:1672–1675. http://dx.doi.org/10.1021/ci050182m

Walker, M.L., S.A. Burgess, J.R. Sellers, F. Wang, J.A. Hammer III, J. Trinick, and P.J. Knight. 2000. Two-headed binding of a processive myosin to F-actin. *Nature.* 405:804–807. http://dx.doi.org/10.1038/35015592